INTERNATIONAL JOURNAL FOR NUMERICAL METHODS IN FLUIDS
Int. J. Numer. Meth. Fluids (2015)
Published online in Wiley Online Library (wileyonlinelibrary.com). DOI: 10.1002/fld.4187

Edge-based reconstruction schemes for unstructured tetrahedral meshes

Ilya Abalakin, Pavel Bakhvalov and Tatiana Kozubskaya*,†

Keldysh Institute of Applied Mathematics, Miusskaya sq., 4, Moscow, 125047, Russia

SUMMARY

In this paper, we consider edge-based reconstruction (EBR) schemes for solving the Euler equations on unstructured tetrahedral meshes. These schemes are based on a high-accuracy quasi-1D reconstruction of variables on an extended stencil along the edge-based direction. For an arbitrary tetrahedral mesh, the EBR schemes provide higher accuracy in comparison with most second-order schemes at rather low computational costs. The EBR schemes are built in the framework of vertex-centered formulation for the point-wise values of variables.

Here, we prove the high accuracy of EBR schemes for uniform grid-like meshes, introduce an economical implementation of quasi-one-dimensional reconstruction and the resulting new scheme of EBR family, estimate the computational costs, and give new verification results. Copyright © 2015 John Wiley & Sons, Ltd.

Received 5 February 2015; Revised 14 September 2015; Accepted 11 October 2015

KEY WORDS: higher-accuracy method; unstructured tetrahedral meshes; finite differences; quasi-1D edge-based reconstruction; Euler equations

1. INTRODUCTION

High accuracy of numerical simulations in aerodynamics and, especially, aeroacoustics has become an indispensable requirement opening the door to industrial applications. The quality of computations is primarily determined by the accuracy of the numerical scheme in use. In the case of unstructured meshes well suitable for the problems with complex multi-body configurations and realistic shapes, the scheme accuracy is still a challenging problem. Attacking it, one should always take into account an appropriate balance between the accuracy and its price in terms of computational costs.

The desire to reach the high accuracy required in engineering has promoted the currently observed progress in the development of very high-order (HO) methods such as finite-volume (FV) polynomial-based Weighted Essentially Non-Oscillatory (WENO), discontinuous Galerkin (DG), and spectral schemes. For smooth solutions, the very HO schemes provide extremely accurate results, for instance, in comparison with Godunov-type schemes of the second order, and undoubtedly are the leaders. However, there are three serious factors that restrict their wide implementation in real aerodynamics and aeroacoustics problems.

First, the meshes for the real applications are inevitably coarse, and the absolute accuracy on such meshes is more important than the order of accuracy, which is evaluated asymptotically. In practice, the absolute errors provided by the very high-order schemes can be comparable with or even exceed the errors of some lower-order schemes on coarse meshes. In the paper, it is shown for the test cases.

*Correspondence to: Tatiana Kozubskaya, Keldysh Institute of Applied Mathematics, Miusskaya sq., 4, Moscow, 125047, Russia.
†E-mail: tatiana.kozubskaya@gmail.com

Second, the desired high accuracy should be balanced with the computational costs needed to reach it. At the current stage, the high cost of the very HO schemes prevents their wide use in solving real-life problems.

Third, for the problems with non-smooth solutions (which are typical for real applications), the development of shock-capturing techniques compatible with the very HO methods still presents a serious difficulty.

In the class of k-exact FV methods possessing very high orders on smooth solutions, the high gradients and discontinuities are mainly supported by introducing the WENO technology. Being firstly proposed as a finite-difference method for Cartesian grids [1, 2], the WENO scheme has been extended to FV approach and unstructured meshes [3, 4]. Further developments of WENO scheme are given, for instance, in [5–8]. In spite of the impressive results presented there, the FV WENO scheme for unstructured meshes remains too heavy to be widely used in engineering, mostly, because of the computationally expensive procedure of multiple calculations of three-dimensional (3D) polynomial coefficients.

According to many discussions on DG schemes (in particular [9–12]), limiters also remain the bottleneck. A difficulty of the rapidly developing spectral methods that are close in a sense to the DG schemes and produce very accurate results for smooth solutions is the elaborate construction of artificial viscosity [13–16]. Resuming, we can say that the development of a scheme providing a stable behavior on discontinuities and a very high accuracy in smooth zones still presents a crucial problem in computational fluid dynamics. As a possible improvement, in [17–20], the authors have proposed a local switching from DG to WENO in the regions of discontinuities. A reverse side of this hybrid approach is the necessity to have a fine and robust indicator (monitor) for such switching.

Thus, to develop a scheme suitable for real applications, we need to look for a compromise between high accuracy, robust shock capturing, and the corresponding computational costs.

From this standpoint, some vertex-centered schemes for unstructured meshes can be of special interest. The flux corrector (FC) scheme [21] proposed in 2011 by A. Katz and V. Sankaran presents a new result in this direction. This scheme possesses the second order of approximation in the point-wise sense for arbitrary unstructured meshes. The main feature of this scheme is the third order of accuracy for steady problems. At the same time, for unsteady problems it exhibits the second order of accuracy even on uniform meshes. Thanks to its robustness and rather low computational costs the FC scheme has been promptly extended to convection-diffusion problems [22] and the Navier–Stokes equations [23–25]. Some authors have proposed modifications of FC scheme which do provide the third order of accuracy for unsteady problems (see, in particular, [24]), however these modifications lead to significant complication of the algorithm and the loss of its conservation property. The papers [26, 27] have presented the techniques of strand meshes when using the FC on unstructured mesh on surfaces tangent to the walls and switching to a high-order finite-difference scheme in the normal direction. Such approach allows one to better treat strong anisotropic curvilinear boundary layers.

The present paper considers another family of vertex-centered schemes, namely, EBR (edge-based reconstruction) schemes, based on a quasi-one-dimensional (1D) edge-oriented reconstruction of variables.[‡] This idea was firstly proposed in the 1990s [28, 29] and then has been developed (for instance [30–32]) as an efficient algorithm providing higher accuracy on unstructured meshes for point-wise values.

Here, we present an interpretation of the EBR schemes in terms of finite differences for irregular meshes. We introduce a concept of translationally symmetric meshes that are uniform grid-like meshes and prove a high accuracy of the EBR schemes for this family of meshes. We show that the underlying high-accuracy scheme for Cartesian meshes keeps its high accuracy for linearly deformed meshes under the EBR approach.

We propose a new efficient implementation of quasi-1D reconstruction techniques and thereby present the new SEBR (simplified EBR) scheme of EBR family optimal in terms of computational

[‡]Here, under the EBR family, we mean all the possible schemes based on the idea of quasi-1D reconstruction of variables. A particular scheme is thus determined by the Riemann solver, the type of reconstructed variables (for instance, physical or flux variables), and, mainly, by the choice of unstructured edge-oriented stencil for the approximation of fluxes. In particular, two schemes of this family, namely, NLV6 and LV6 schemes are presented in [32]. The FC scheme [21] with a special approximation of nodal gradients can be also considered as an EBR scheme.

DOI: 10.1002/fld

costs. We estimate the computational costs of different EBR schemes in comparison with the quadratic-polynomial-based FV method and the FC scheme.

Finally, we give new verification results for the two-dimensional (2D) Rankine vortex and 3D Gaussian pulse and show the examples of problems solved by the EBR schemes.

Note that, in this paper, we consider only smooth solutions. Because of the limitations on the volume of the paper, we do not discuss here results for shocks. We have developed a WENO-based extension of EBR schemes to discontinuities, which will be presented in detail in the forthcoming paper.

2. BASIC 1D HIGH ACCURACY SCHEME

2.1. Scheme for the linear transport equation on uniform meshes

Let us consider the linear transport equation

$$\frac{\partial u}{\partial t} + a\frac{\partial u}{\partial x} = 0, \quad a > 0. \tag{1}$$

According to the method of lines, the semi-discrete approximation of Equation (1) can be written as the ordinary differential equation (ODE)

$$\left(\frac{du}{dt}\right)_j = -\Psi_j(u),$$

where the function $\Psi_j(u) = a\left[\frac{\partial u}{\partial x}\right]_j^L$ is an approximation of the space derivative. Superscript L denotes the upwind approximation of the gradient using the stencil skewed to the left.

Let us now introduce the uniform mesh with nodes x_j and the constant mesh step $\Delta x = x_{j+1} - x_j$ for all j. The computational cell for the node j is defined as the segment with the boundaries $x_{j\mp 1/2} = x_j \mp \Delta x/2$. The unknown function is defined in the mesh nodes: $u_j = u(x_j)$.

We approximate the space derivative as

$$\Psi_j(u) = a\frac{-2u_{j-3} + 15u_{j-2} - 60u_{j-1} + 20u_j + 30u_{j+1} - 3u_{j+2}}{60\Delta x}. \tag{2}$$

Using the Taylor expansion, one can see that formula (2) provides the fifth order of accuracy. Approximation (2) can be also presented in the divergent form

$$\Psi_j(u) = a\frac{u^L_{j+1/2} - u^L_{j-1/2}}{\Delta x} \tag{3a}$$

with the reconstructed values of unknown function u at the interface points $x_{j\pm 1/2}$ written in terms of first finite differences:

$$\begin{aligned} u^L_{j+1/2} &= u_j + \frac{1}{2}\left(-\frac{1}{15}\Delta u_{j-3/2} + \frac{11}{30}\Delta u_{j-1/2} + \frac{4}{5}\Delta u_{j+1/2} - \frac{1}{10}\Delta u_{j+3/2}\right) \\ u^L_{j-1/2} &= u_{j-1} + \frac{1}{2}\left(-\frac{1}{15}\Delta u_{j-5/2} + \frac{11}{30}\Delta u_{j-3/2} + \frac{4}{5}\Delta u_{j-1/2} - \frac{1}{10}\Delta u_{j+1/2}\right) \end{aligned} \tag{3b}$$

where $\Delta u_{k+1/2} = u_{k+1} - u_k$.

If the advection velocity is negative, that is, $a < 0$, the corresponding fifth-order approximation takes the form

DOI: 10.1002/fld

$$\Psi_j(u) = a\left[\frac{\partial u}{\partial x}\right]_j^R = a\frac{u^R_{j+1/2} - u^R_{j-1/2}}{\Delta x}, \tag{4a}$$

where the reconstructed values $u^R_{j\pm1/2}$ are defined as

$$\begin{aligned} u^R_{j+1/2} &= u_{j+1} - \frac{1}{2}\left(-\frac{1}{10}\Delta u_{j-1/2} + \frac{4}{5}\Delta u_{j+1/2} + \frac{11}{30}\Delta u_{j+3/2} - \frac{1}{15}\Delta u_{j+5/2}\right) \\ u^R_{j-1/2} &= u_j - \frac{1}{2}\left(-\frac{1}{10}\Delta u_{j-3/2} + \frac{4}{5}\Delta u_{j-1/2} + \frac{11}{30}\Delta u_{j+1/2} - \frac{1}{15}\Delta u_{j+3/2}\right). \end{aligned} \tag{4b}$$

Here, superscript R denotes the upwind approximation of the gradient using the stencil skewed to the right.

2.2. *Scheme for the linear transport equation on non-uniform meshes*

In the case of a non-uniform mesh with nodes x_j and mesh steps $\Delta x_{j+1/2} = x_{j+1} - x_j$, the computational cell for the node j is defined as the segment with the boundaries $x_{j-1/2} = (x_{j-1} + x_j)/2$ and $x_{j+1/2} = (x_j + x_{j+1})/2$ and the length $\hbar_j = x_{j+1/2} - x_{j-1/2}$.

We build the higher-accuracy scheme of (3a) and (3b) or (4a) and (4b) as follows:

$$\Psi_j(u) = a\left[\frac{\partial u}{\partial x}\right]_j^{L/R} = a\frac{u^{L/R}_{j+1/2} - u^{L/R}_{j-1/2}}{\hbar_j}, \tag{5a}$$

where the reconstructed values $u^{L/R}_{j+1/2}$ are defined as

$$\begin{aligned} u^L_{j+1/2} &= u_j + \frac{\Delta x_{j+1/2}}{2}\left(-\frac{1}{15}\frac{\Delta u_{j-3/2}}{\Delta x_{j-3/2}} + \frac{11}{30}\frac{\Delta u_{j-1/2}}{\Delta x_{j-1/2}} + \frac{4}{5}\frac{\Delta u_{j+1/2}}{\Delta x_{j+1/2}} - \frac{1}{10}\frac{\Delta u_{j+3/2}}{\Delta x_{j+3/2}}\right) \\ u^R_{j+1/2} &= u_{j+1} - \frac{\Delta x_{j+1/2}}{2}\left(-\frac{1}{10}\frac{\Delta u_{j-1/2}}{\Delta x_{j-1/2}} + \frac{4}{5}\frac{\Delta u_{j+1/2}}{\Delta x_{j+1/2}} + \frac{11}{30}\frac{\Delta u_{j+3/2}}{\Delta x_{j+3/2}} - \frac{1}{15}\frac{\Delta u_{j+5/2}}{\Delta x_{j+5/2}}\right). \end{aligned} \tag{5b}$$

We can also consider the scheme on the reduced 3-points stencil as

$$\begin{aligned} u^L_{j+1/2} &= u_j + \frac{\Delta x_{j+1/2}}{2}\left(\frac{1}{3}\frac{\Delta u_{j-1/2}}{\Delta x_{j-1/2}} + \frac{2}{3}\frac{\Delta u_{j+1/2}}{\Delta x_{j+1/2}}\right) \\ u^R_{j+1/2} &= u_{j+1} - \frac{\Delta x_{j+1/2}}{2}\left(\frac{2}{3}\frac{\Delta u_{j+1/2}}{\Delta x_{j+1/2}} + \frac{1}{3}\frac{\Delta u_{j+3/2}}{\Delta x_{j+3/2}}\right). \end{aligned} \tag{5c}$$

To define the values $u^{L/R}_{j-1/2}$, we apply the same procedure of reconstruction. Thus, for non-uniform meshes we use the same coefficients in front of divided differences as in the uniform-mesh reconstruction.

Such definition of the reconstructed variables on the non-uniform mesh guarantees the following two important properties:

1. Formulas (5b) coincide with the high-accuracy reconstruction (3b), (4b) on uniform meshes;
2. Formulas (5b) provide the exactness on linear functions of values $u^L_{j+1/2}$ and $u^R_{j+1/2}$ in interface points $x_{j+1/2}$.

We remark here that (5b) is not the only possible way of reconstruction on non-uniform meshes, which provides these two properties.

DOI: 10.1002/fld

2.3. Scheme for nonlinear equations

Consider the 1D hyperbolic system of conservation laws

$$\frac{\partial \mathbf{Q}}{\partial t} + \frac{\partial \mathbf{F}(\mathbf{Q})}{\partial x} = 0. \tag{6}$$

The general formulation of an upwind scheme for Equation (6) can be written as

$$\left(\frac{d\mathbf{Q}}{dt}\right)_j + \frac{h_{j+1/2}\left(\mathbf{F}^R_{j+1/2},\ \mathbf{F}^L_{j+1/2},\ \mathbf{Q}^R_{j+1/2},\ \mathbf{Q}^L_{j+1/2}\right) - h_{j-1/2}\left(\mathbf{F}^R_{j-1/2},\ \mathbf{F}^L_{j-1/2},\ \mathbf{Q}^R_{j-1/2},\ \mathbf{Q}^L_{j-1/2}\right)}{\left(\Delta x_{j+1/2} + \Delta x_{j-1/2}\right)/2} = 0, \tag{7}$$

where $\mathbf{Q}^L_{j\pm1/2}$ and $\mathbf{Q}^R_{j\pm1/2}$ are the values of conservative variables reconstructed from the left and right sides (notations L and R, respectively, see (5b)) with respect to the computational cell boundaries $x_{j\pm1/2}$, $\mathbf{F}^L_{j\pm1/2}$ and $\mathbf{F}^R_{j\pm1/2}$ are reconstructed flux variables. $h(\ldots)$ is the numerical flux defined by some Riemann solver.

For instance, in [32], the scheme LV6 or MUSCLV6 on unstructured meshes is based on the Roe solver [33] disregarding the values of reconstructed fluxes:

$$h^{Roe}\left(\mathbf{Q}^R_{j\pm1/2}, \mathbf{Q}^L_{j\pm1/2}\right) = \frac{\mathbf{F}\left(\mathbf{Q}^R_{j\pm1/2}\right) + \mathbf{F}\left(\mathbf{Q}^L_{j\pm1/2}\right)}{2} - \frac{\delta}{2}\left|\frac{d\mathbf{F}}{d\mathbf{Q}}\left(\mathbf{Q}^{Roe}_{j\pm1/2}\right)\right|\left(\mathbf{Q}^R_{j\pm1/2} - \mathbf{Q}^L_{j\pm1/2}\right). \tag{8}$$

Here, the parameter δ controls the scheme dissipation: $0 \leqslant \delta \leqslant 1$. Within the family of schemes (8) for nonlinear hyperbolic equations, there exist no schemes of accuracy higher than that of the second order in the point-wise sense even on uniform meshes [34]. To overcome this barrier, the authors of [32] presented NLV6 scheme based on the 1D solver of Huang [35]:

$$h^{Huang}\left(\mathbf{F}^R_{j\pm1/2}, \mathbf{F}^L_{j\pm1/2}\right) = \frac{\mathbf{F}^R_{j\pm1/2} + \mathbf{F}^L_{j\pm1/2}}{2} - \frac{\delta}{2}\,\mathrm{sign}\left(\frac{d\mathbf{F}}{d\mathbf{Q}}\left(\mathbf{Q}_{j\pm1/2}\right)\right)\left(\mathbf{F}^R_{j\pm1/2} - \mathbf{F}^L_{j\pm1/2}\right). \tag{9}$$

In contrast to (8), in this scheme, we reconstruct the fluxes $\mathbf{F}^L_{j\pm1/2}$ and $\mathbf{F}^R_{j\pm1/2}$ using the same formulae (5b) as for the reconstruction of variables. The finite-difference scheme (7), (9) with the flux reconstruction (5b) possesses the fifth order of accuracy on uniform meshes and transforms to the sixth-order central-difference scheme if $\delta = 0$. However, this scheme can cause instability near physical boundaries. So there we switch to the reconstruction of conservative variables (7), (8).

A more robust algorithm that also provides the fifth to sixth order of accuracy on uniform meshes is obtained if we use the reconstructed values both for variables and fluxes:

$$h^{Roe}\left(\mathbf{F}^R_{j\pm1/2}, \mathbf{F}^L_{j\pm1/2}, \mathbf{Q}^R_{j\pm1/2}, \mathbf{Q}^L_{j\pm1/2}\right) = \frac{\mathbf{F}^R_{j\pm1/2} + \mathbf{F}^L_{j\pm1/2}}{2} - \frac{\delta}{2}\left|\frac{d\mathbf{F}}{d\mathbf{Q}}\left(\mathbf{Q}^{Roe}_{j\pm1/2}\right)\right|\left(\mathbf{Q}^R_{j\pm1/2} - \mathbf{Q}^L_{j\pm1/2}\right). \tag{10}$$

This way is slightly more expensive than schemes (7), (8) and (7), (9) because of a larger number of reconstructions. However, in some cases, it provides a more stable computation.

Unless otherwise specified later on we imply the Riemann solver of Huang type (9) and, correspondingly, the reconstruction of fluxes, as it is in NLV6 [32].

DOI: 10.1002/fld

3. EDGE-BASED RECONSTRUCTION SCHEMES FOR UNSTRUCTURED MESHES

3.1. Basic conservative vertex-centered formulation

In the case of vertex-centered algorithms considered in the paper, the physical or conservative variables are defined in the mesh nodes. The construction of a conservative scheme requires to define control volumes, or cells, used to discretize conservation laws.

The Euler system written for the conservative variables $\mathbf{Q}=(\rho,\ \rho u,\ \rho v,\ \rho w,\ E)^T$ is

$$\frac{\partial \mathbf{Q}}{\partial t}+\frac{\partial \mathbf{F}(\mathbf{Q})}{\partial x}+\frac{\partial \mathbf{G}(\mathbf{Q})}{\partial y}+\frac{\partial \mathbf{H}(\mathbf{Q})}{\partial z}=0$$

$$\mathbf{F}=\begin{pmatrix}\rho u\\ \rho u^2+p\\ \rho uv\\ \rho uw\\ u(E+p)\end{pmatrix},\quad \mathbf{G}=\begin{pmatrix}\rho v\\ \rho uv\\ \rho v^2+p\\ \rho vw\\ v(E+p)\end{pmatrix},\quad \mathbf{H}=\begin{pmatrix}\rho w\\ \rho uw\\ \rho vw\\ \rho w^2+p\\ w(E+p)\end{pmatrix}.$$

The conservation law for this system is

$$\frac{d\overline{\mathbf{Q}}_i}{dt}=-\frac{1}{|C_i|}\int\limits_{\partial C_i}(\mathcal{F}\cdot\mathbf{n})\,ds,\quad \mathcal{F}=(\mathbf{F},\mathbf{G},\mathbf{H}),\tag{15}$$

where C_i is the cell of node i, $|C_i|$ is its volume, ∂C_i is its boundary, $\mathbf{n}=(n_x,n_y,n_z)$ is the outward unit normal to the cell boundary, and $\overline{\mathbf{Q}}_i$ is the integral average of $\mathbf{Q}$ over the cell C_i.

In this paper, we use two types of cells: barycentric and orthocentric. Barycentric cells are built on the basis of the gravity centers of tetrahedrons, their triangular faces and edges in the 3D case, and gravity centers of triangles and edge centers in the 2D case. The supporting points for orthocentric cells are the circumcenters of tetrahedrons, triangles, and edge centers.

The cell surface can be represented as $\partial C_i=\bigcup\limits_{k\in N_1(i)}\partial C_{ik}$ where $N_1(i)$ is the set of the mesh nodes neighboring (i.e., connected by a single edge) with the vertex i and ∂C_{ik} is (generally) polyhedral cell face separating the nodes i and k.

To approximate (15), we substitute $\mathbf{Q}_i$ (point values of $\mathbf{Q}$ in mesh nodes) for $\overline{\mathbf{Q}}_i$. Then we write

$$\int\limits_{\partial C_i}(\mathcal{F}\cdot\mathbf{n})\,ds=\sum_{k\in N_1(i)}\int\limits_{\partial C_{ik}}(\mathcal{F}\cdot\mathbf{n})\,ds\approx\sum_{k\in N_1(i)}\mathbf{h}_{ik},$$

where $\mathbf{h}_{ik}$ is the numerical flux that approximates the flux through the cell face ik. Thus, the particular scheme formulation is reduced to the definition of the numerical fluxes $\mathbf{h}_{ik}$.

Let us define $\mathbf{h}_{ik}=\mathcal{F}_{ik}\cdot\mathbf{n}_{ik}$ where $\mathcal{F}_{ik}$ is flux value taken at the point of intersection of the face ∂C_{ik} with the mesh edge ik (this point is the middle of the edge ik) and $\mathbf{n}_{ik}=\int\limits_{\partial C_{ik}}\mathbf{n}\,ds$ is the sum of oriented areas of all the subfaces composing the face ∂C_{ik}.

We call the resulting scheme

$$\left(\frac{d\mathbf{Q}}{dt}\right)_i=-\frac{1}{|C_i|}\sum_{k\in N_1(i)}\mathbf{h}_{ik}\tag{16}$$

DOI: 10.1002/fld

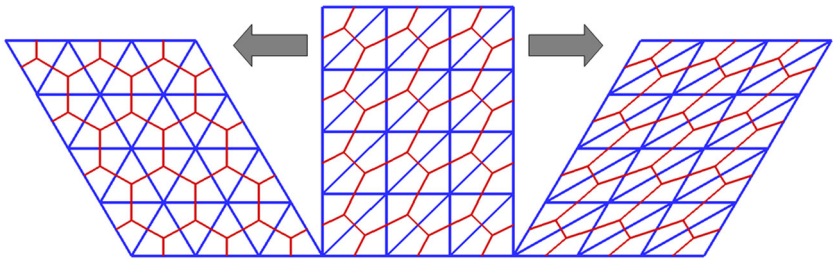

Figure 1. Translationally symmetric meshes (in blue) with barycentric cells (in red).

an *edge-based reconstruction scheme* if the fluxes $\mathbf{h}_{ik}$ are found with the help of a 1D reconstruction procedure along the corresponding mesh edge [36]. The details of such reconstruction in the case of triangular/tetrahedral meshes are considered further.

3.2. EBR schemes on translationally symmetric triangular/tetrahedral meshes

We introduce a special class of meshes as follows.

Definition 1

A mesh is said to be *translationally symmetric* if it is translationally invariant with respect to the vectors of all edges of the mesh.

Translationally symmetric meshes (or TS-meshes) have uniform lattice structure; their examples (together with cells drawn in red) in 2D case are shown in Figure 1. We can see that triangular TS-meshes are built by linear transformations of rectangles decomposed in two triangles in a uniform manner.

Analogously, in 3D case, any tetrahedral TS-mesh is a linear transformation of cubes decomposed uniformly into six tetrahedrons. Note that the cubic mesh can be uniformly decomposed into six tetrahedrons only in two different ways[§] [37]. In both cases, a set of tetrahedrons included in the cube is characterized by seven different edges, so that the mesh remains the same with respect to the translation by each of them.

In 2D, all the edges of any translational symmetric triangular mesh form three families of equal-spaced parallel straight lines. In 3D, the tetrahedral TS-mesh structure is described by six families of parallel planes. An important property of the TS-mesh is that its nodes are located on straight lines at equal distances.

Let us build an EBR scheme for TS-meshes. To form an Mth-order scheme, we need the difference of fluxes through the opposite faces ∂C_{ik} and $\partial C_{\underset{\sim}{ik}}$ to approximate the gradient of the function $\mathcal{F}\cdot\mathbf{n}_{ik}$ in the node i multiplied by the vector $\mathbf{e}_{ik}=\mathbf{r}_k-\mathbf{r}_i$:

$$\mathbf{h}_{ik}-\mathbf{h}_{\underset{\sim}{ik}}=\frac{\partial\mathcal{F}\cdot\mathbf{n}_{ik}}{\partial x^m}e_{ik}^m+O\left(|\mathbf{e}_{ik}|^{M+1}|\mathbf{n}_{ik}|\right) \tag{17}$$

where $\mathbf{r}_i$ and $\mathbf{r}_k$ are the radius-vectors of vertices i and k.

The simplest way to satisfy (17) is a direct implementation of high-accuracy 1D-reconstruction (3b–4b) based on the mesh nodes on the straight line containing the edge ik (Figure 2). To determine the numerical flux $\mathbf{h}_{ik}$ at the middles of mesh edges in (16), we use one of the Riemann solvers ((8) in linear case, (9), (10) or some others), where the values of variables/fluxes taken from

[§]Under uniform decomposition of a cubic mesh we mean the decomposition when all the cubes are decomposed in the same way that provides translational symmetry of the resulting tetrahedral mesh. To implement this, it is sufficient to provide the same-oriented diagonal decomposition of all the opposite faces in each cube. Up to reflection and rotation, there are only two possible techniques of decomposition: In the first case, all the tetrahedrons inside each cube have one common edge (New Generation Division (NGD) decomposition); in the second case, the tetrahedrons inside each cube have no edge common for all of them. Both types of decomposition result in topologically equivalent meshes.

DOI: 10.1002/fld

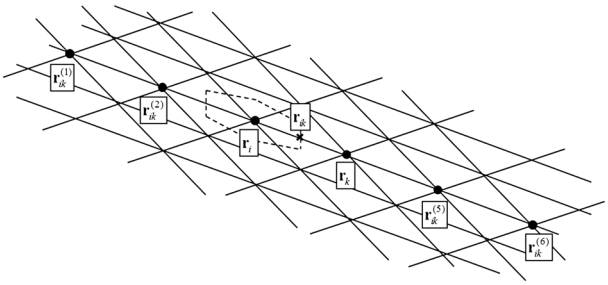

Figure 2. The 6-points stencil for the one-dimensional high-accuracy reconstruction of flux variables.

different sides of the cell interface are found from the 1D high-accuracy reconstruction (3b–4b) along the corresponding edge-based direction.

Note that the condition (17) can be satisfied even when not all the nodes involved in the reconstruction are located on the edge-based straight line. An example is the NLV6 scheme [32] where the numerical flux $\mathbf{h}_{ik}$ is approximated with the help of nodal gradients.

Thus, for the vertex i, the values $\mathbf{h}_{ik}$ are calculated based on 6-points stencils $S_{ik}^{1D} = \left\{\mathbf{r}_{ik}^{(1)},\ \mathbf{r}_{ik}^{(2)},\ \mathbf{r}_{ik}^{(3)} \equiv \mathbf{r}_i,\ \mathbf{r}_{ik}^{(4)} \equiv \mathbf{r}_k,\ \mathbf{r}_{ik}^{(5)},\ \mathbf{r}_{ik}^{(6)}\right\}$. The stencil points $\left\{\mathbf{r}_{ik}^{(s)},\ s = 1,2,5,6\right\}$ are the mesh nodes lying on the straight line passing the vertices i and k from both sides of them (Figure 2).

Denote the values of the flux function $\mathcal{F}\cdot\mathbf{n}_{ik}$ at the points $\mathbf{r}_{ik}^{(s)},\ s = \overline{1,6}$ by $\mathbf{\Phi}_{ik}^{(s)}$. Then the numerical flux $\mathbf{h}_{ik}$ can be found as a function $\mathbf{h}_{ik}\left(\mathbf{\Phi}_{ik}^{L}, \mathbf{\Phi}_{ik}^{R}\right)$ of the flux variables $\mathbf{\Phi}_{ik}^{L}, \mathbf{\Phi}_{ik}^{R}$ reconstructed from both sides of the interface point $\mathbf{r}_{ik}$ (Figure 2). The 1D high accuracy reconstruction of the flux variables $\mathbf{\Phi}_{ik}^{L}$, $\mathbf{\Phi}_{ik}^{R}$ according to (3b), (4b) can be written in the form

$$\mathbf{\Phi}_{ik}^{L} = \mathbf{\Phi}_i + \frac{1}{2}\left(-\frac{1}{15}\Delta\mathbf{\Phi}_{ik}^{(3/2)} + \frac{11}{30}\Delta\mathbf{\Phi}_{ik}^{(5/2)} + \frac{4}{5}\Delta\mathbf{\Phi}_{ik}^{(7/2)} - \frac{1}{10}\Delta\mathbf{\Phi}_{ik}^{(9/2)}\right)$$

$$\mathbf{\Phi}_{ik}^{R} = \mathbf{\Phi}_k - \frac{1}{2}\left(-\frac{1}{10}\Delta\mathbf{\Phi}_{ik}^{(5/2)} + \frac{4}{5}\Delta\mathbf{\Phi}_{ik}^{(7/2)} + \frac{11}{30}\Delta\mathbf{\Phi}_{ik}^{(9/2)} - \frac{1}{15}\Delta\mathbf{\Phi}_{ik}^{(11/2)}\right)$$

where $\Delta\mathbf{\Phi}_{ik}^{(s+1/2)}$ denotes the finite differences $\Delta\mathbf{\Phi}_{ik}^{(s+1/2)} = \mathbf{\Phi}_{ik}^{(s+1)} - \mathbf{\Phi}_{ik}^{(s)}$. The function $\mathbf{h}_{ik}\left(\mathbf{\Phi}_{ik}^{L}, \mathbf{\Phi}_{ik}^{R}\right)$ is determined by the Huang solver (9).

3.3. Accuracy of EBR schemes on translationally symmetric triangular/tetrahedral mesh

Now, we are in position to prove that TS-meshes provide the highest theoretically reachable order of EBR schemes.

Proposition

On translational symmetric meshes with a uniform method of cell construction for each vertex, the EBR schemes possess the accuracy of order M, where M is the width of the corresponding stencil of reconstruction (i.e., the stencil consists of $\mathrm{M}+1$ mesh nodes).

Proof

For TS-meshes, the boundary ∂C_i of the control volume C_i consists of couples of opposite faces ∂C_{ik} and $\partial C_{i\tilde{k}}$ between the vertex i and the opposite neighboring vertices k and $\widetilde{k}$. The oriented areas $\mathbf{n}_{ik} \curlywedge \mathbf{n}_{\widetilde{ik}}$ corresponding to the opposite faces ∂C_{ik} and $\partial C_{i\tilde{k}}$ are also opposite: $\mathbf{n}_{i\tilde{k}} = -\mathbf{n}_{ik}$. Take one face from each couple $\left\{\partial C_{ik}, \partial C_{\widetilde{ik}}\right\}$ and denote the resulting set by $N_1(i)/2$.

DOI: 10.1002/fld

Let $\mathbf{r}_i$, $\mathbf{r}_k$, $\mathbf{r}\widetilde{k}$ be the radius-vectors of vertices i, k, $\widetilde{k}$. Define the directions of reconstruction as $\mathbf{e}_{ik}=\mathbf{r}_k-\mathbf{r}_i$.

Here and below we assume the summation over repeated superscripts.

According to (17), the approximation of the divergence operator in the node i takes the form

$$\left[\frac{\partial \mathcal{F}^j}{\partial x^j}\right]_i=\frac{1}{|C_i|}\sum_{k\in N_1(i)/2} n_{ik}^m \mathbf{e}_{ik}^j \left.\frac{\partial \mathcal{F}^m}{\partial x^j}\right|_{r=r_i}+O\left(\frac{\sum\limits_{k\in N_1(i)/2}|\mathbf{n}_{ik}||\mathbf{e}_{ik}|^{M+1}}{|C_i|}\right) \tag{18}$$

Thus, to satisfy the condition on the high order of approximation

$$\left[\frac{\partial \mathcal{F}^m}{\partial x^m}\right]_i=\left.\frac{\partial \mathcal{F}^m}{\partial x^m}\right|_{r=r_i}+O\left(\frac{\sum\limits_{k\in N_1(i)}|\mathbf{n}_{ik}||\mathbf{e}_{ik}|^{M+1}}{|C_i|}\right), \tag{19}$$

the following equality

$$\frac{1}{|C_i|}\sum_{k\in N_1(i)/2} n_{ik}^m \mathbf{e}_{ik}^j=\delta^{mj}=\begin{cases}1, & j=m\\ 0, & j\neq m\end{cases} \tag{20}$$

is necessary and sufficient on a TS-mesh.

Let us prove (20). Introduce the radius-vector $\mathbf{r}_{ik}=\left(x_{ik}^1,x_{ik}^2,x_{ik}^3\right)$ of the mass center of the face ∂C_{ik}

$$\mathbf{r}_{ik}=\frac{1}{|\mathbf{n}_{ik}|}\int\limits_{\partial C_{ik}}\mathbf{r}ds.$$

Using the Gauss–Ostrogradsky theorem, we can express the derivative of an arbitrary linear function $u(\mathbf{r})=\mathbf{L}\cdot\mathbf{r}=L^m x^m$ as follows:

$$L^m=\frac{1}{|C_i|}\int\limits_{\partial C_i} n^m(\mathbf{r})\,u(\mathbf{r})ds=L^j\left(\frac{1}{|C_i|}\sum_{k\in N_1(i)}\int\limits_{\partial C_{ik}} n^m x^j ds\right).$$

From here, it immediately follows that $\sum\limits_{k\in N_1(i)}\int\limits_{\partial C_{ik}} n_{ik}^m x^j ds=|C_i|\delta^{mj}$. Because the boundary of the control volume consists of couples of opposite faces, we can reformulate it as

$$|C_i|\delta^{mj}=\sum_{k\in N_1(i)/2}\left(\int\limits_{\partial C_{ik}} n^m x^j ds+\int\limits_{\partial C_{i\widetilde{k}}} n^m x^j ds\right).$$

Because the opposite faces are equal up to the translation on the vector $\mathbf{e}_{ik}=\mathbf{r}_k-\mathbf{r}_i$, we can write the following:

DOI: 10.1002/fld

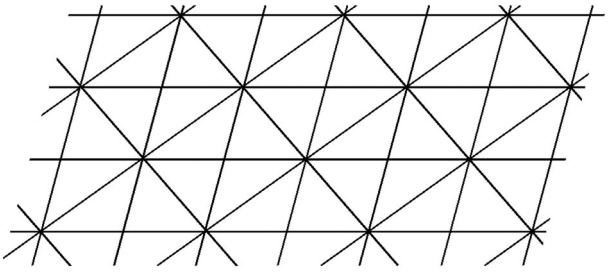

Figure 3. Example of a non-translationally symmetric mesh on which edge-based reconstruction schemes reach the highest theoretically possible order of accuracy.

$$|C_i|\delta^{mj} = \sum_{k \in N_1(i)/2} \left(\int_{\partial C_{ik}} n^m x^j ds + \int_{\partial C_{ik}} (-n^m)\left(x^j - \mathrm{e}_{ik}^j\right) ds \right) = \sum_{k \in N_1(i)/2} \int_{\partial C_{ik}} n^m \mathrm{e}_{ik}^j ds = \sum_{k \in N_1(i)/2} \mathrm{e}_{ik}^j n_{ik}^m$$

which proves (20) and, therefore, the whole Proposition.

Note that there are meshes formally different from TS-meshes where the nodes are also located on straight lines at equal distances (for example, Figure 3). On such meshes, EBR schemes possess the accuracy of order M only on barycentric cells. This fact can be easily proved because the formula (17) remains valid and (20) holds on barycentric cells for arbitrary unstructured meshes.

3.4. EBR scheme on an arbitrary triangular/tetrahedral mesh

3.4.1. 1D reconstruction. In the case of an arbitrary triangular or tetrahedral mesh, the direction of the flux variable reconstruction is also based on the edge direction, that is, the direction **E** containing the edge *ik* in Figure 4.

The choice of the stencil of reconstruction in the arbitrary unstructured case is not so obvious. Let us describe the procedure of stencil definition on the example of a triangular mesh. The procedure is

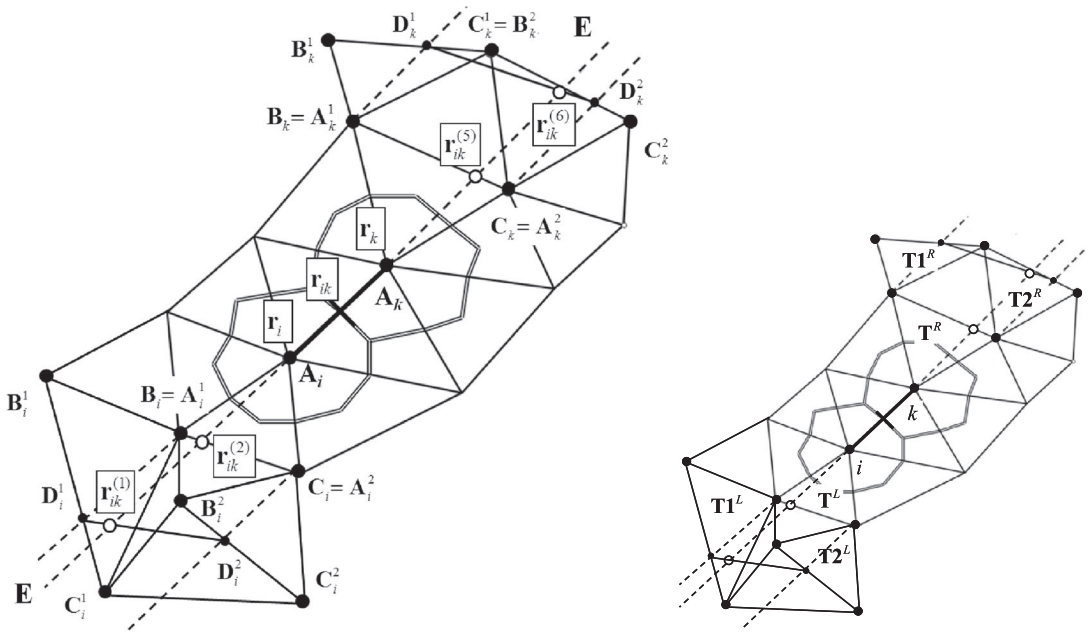

Figure 4. Definition of the reconstruction direction and stencil points for an arbitrary triangular mesh.

DOI: 10.1002/fld

illustrated in Figure 4. The point $\mathbf{r}_{ik}^{(5)}$ is found at the intersection of line $\mathbf{E}$ with the edge $[\mathrm{B}_k\mathrm{C}_k]$ of the triangle $\mathrm{A}_k\mathrm{B}_k\mathrm{C}_k$. The point $\mathbf{r}_{ik}^{(6)}$ lies at the intersection of line $\mathbf{E}$ with the segment $\left[D_k^1 D_k^2\right]$ where the points D_k^1 and D_k^2 are the intersections of lines parallel to $\mathbf{E}$ and passing the vertices A_k^1 and A_k^2 with the edges $\left[B_k^1 C_k^1\right]$ and $\left[B_k^2 C_k^2\right]$, correspondingly. The points $\mathbf{r}_{ik}^{(1)}$ and $\mathbf{r}_{ik}^{(2)}$ are found from a similar geometrical construction to the left from the vertex $\mathbf{r}_i$, which involves the triangles $\mathrm{A}_i\mathrm{B}_i\mathrm{C}_i$, $A_i^1 B_i^1 C_i^1$, and $A_i^2 B_i^2 C_i^2$.

Analogously to the formula for 1D non-uniform meshes (5b), we introduce the procedure of 1D reconstruction of the function $\mathbf{\Phi}_{ik}$ along the line $\mathbf{E}$ as

$$\begin{aligned}
\mathbf{\Phi}_{ik}^L &= \mathbf{\Phi}_i + \frac{\Delta r_{ik}^{(7/2)}}{2}\left(-\frac{1}{15}\frac{\Delta\mathbf{\Phi}_{ik}^{(3/2)}}{\Delta r_{ik}^{(3/2)}} + \frac{11}{30}\frac{\Delta\mathbf{\Phi}_{ik}^{(5/2)}}{\Delta r_{ik}^{(5/2)}} + \frac{4}{5}\frac{\Delta\mathbf{\Phi}_{ik}^{(7/2)}}{\Delta r_{ik}^{(7/2)}} - \frac{1}{10}\frac{\Delta\mathbf{\Phi}_{ik}^{(9/2)}}{\Delta r_{ik}^{(9/2)}}\right)\\
\mathbf{\Phi}_{ik}^R &= \mathbf{\Phi}_k - \frac{\Delta r_{ik}^{(7/2)}}{2}\left(-\frac{1}{10}\frac{\Delta\mathbf{\Phi}_{ik}^{(5/2)}}{\Delta r_{ik}^{(5/2)}} + \frac{4}{5}\frac{\Delta\mathbf{\Phi}_{ik}^{(7/2)}}{\Delta r_{ik}^{(7/2)}} + \frac{11}{30}\frac{\Delta\mathbf{\Phi}_{ik}^{(9/2)}}{\Delta r_{ik}^{(9/2)}} - \frac{1}{15}\frac{\Delta\mathbf{\Phi}_{ik}^{(11/2)}}{\Delta r_{ik}^{(11/2)}}\right)
\end{aligned} \tag{21a}$$

where $\Delta r_{ik}^{(s+1/2)} = \left|\mathbf{r}_{ik}^{(s+1)} - \mathbf{r}_{ik}^{(s)}\right|$, $s = 1, \ldots, 5$.

We can also determine a lower-accuracy 1D reconstruction of $\mathbf{\Phi}_{ik}$ along the line $\mathbf{E}$ as

$$\begin{aligned}
\mathbf{\Phi}_{ik}^L &= \mathbf{\Phi}_i + \frac{\Delta r_{ik}^{(7/2)}}{2}\left(\frac{1}{3}\frac{\Delta\mathbf{\Phi}_{ik}^{(5/2)}}{\Delta r_{ik}^{(5/2)}} + \frac{2}{3}\frac{\Delta\mathbf{\Phi}_{ik}^{(7/2)}}{\Delta r_{ik}^{(7/2)}}\right)\\
\mathbf{\Phi}_{ik}^R &= \mathbf{\Phi}_k - \frac{\Delta r_{ik}^{(7/2)}}{2}\left(\frac{2}{3}\frac{\Delta\mathbf{\Phi}_{ik}^{(7/2)}}{\Delta r_{ik}^{(7/2)}} + \frac{1}{3}\frac{\Delta\mathbf{\Phi}_{ik}^{(9/2)}}{\Delta r_{ik}^{(9/2)}}\right)
\end{aligned} \tag{21b}$$

The points $S_{ik}^{1D} = \left\{\mathbf{r}_{ik}^{(1)},\ \mathbf{r}_{ik}^{(2)},\ \mathbf{r}_{ik}^{(3)} \equiv \mathbf{r}_i,\ \mathbf{r}_{ik}^{(4)} \equiv \mathbf{r}_k,\ \mathbf{r}_{ik}^{(5)},\ \mathbf{r}_{ik}^{(6)}\right\}$ define the stencil of *1D reconstruction*. Generally speaking, these points do not coincide with the mesh nodes and therefore cannot be considered as a reconstruction stencil for an arbitrary unstructured mesh. So the divided differences $\frac{\Delta\mathbf{\Phi}_{ik}}{\Delta r_{ik}}$ in (21a), (21b) need a special definition, which is given in the next section.

3.4.2. Unstructured analogs of divided differences. Define the edge vector $\mathbf{e}_{ik} = \mathbf{r}_k - \mathbf{r}_i$. For the geometrical configuration in Figure 4 introduce the *supporting* triangles

$$\begin{array}{lll}
\mathbf{T}1^L = A_i^1 B_i^1 C_i^1 & & \mathbf{T}1^R = A_k^1 B_k^1 C_k^1\\
\mathbf{T}2^L = A_i^2 B_i^2 C_i^2 & \mathbf{T}^L = A_i B_i C_i \quad \mathbf{T}^R = A_k B_k C_k & \mathbf{T}2^R = A_k^2 B_k^2 C_k^2
\end{array}.$$

Let us replace the divided differences in (21a) with P1 Galerkin gradients defined on the triangles[¶] introduced previously and projected onto the line $\mathbf{E}$ as

$$\begin{aligned}
&\frac{\Delta\mathbf{\Phi}_{ik}^{(3/2)}}{\Delta r_{ik}^{(3/2)}} = \left[\sigma_i\nabla\mathbf{\Phi}|_{\mathrm{T}1^L} + (1-\sigma_i)\nabla\mathbf{\Phi}|_{\mathrm{T}2^L}\right]\cdot\frac{\mathbf{e}_{ik}}{|\mathbf{e}_{ik}|},\\
&\frac{\Delta\mathbf{\Phi}_{ik}^{(5/2)}}{\Delta r_{ik}^{(5/2)}} = \nabla\mathbf{\Phi}|_{\mathrm{T}^L}\cdot\frac{\mathbf{e}_{ik}}{|\mathbf{e}_{ik}|}, \quad \Delta\mathbf{\Phi}_{ik}^{(7/2)} = \mathbf{\Phi}_k - \mathbf{\Phi}_i, \quad \frac{\Delta\mathbf{\Phi}_{ik}^{(9/2)}}{\Delta r_{ik}^{(9/2)}} = \nabla\mathbf{\Phi}|_{\mathrm{T}^R}\cdot\frac{\mathbf{e}_{ik}}{|\mathbf{e}_{ik}|},\\
&\frac{\Delta\mathbf{\Phi}_{ik}^{(11/2)}}{\Delta r_{ik}^{(11/2)}} = \left[\sigma_k\nabla\mathbf{\Phi}|_{\mathrm{T}1^R} + (1-\sigma_k)\nabla\mathbf{\Phi}|_{\mathrm{T}2^R}\right]\cdot\frac{\mathbf{e}_{ik}}{|\mathbf{e}_{ik}|}
\end{aligned} \tag{22}$$

[¶]P1 Galerkin gradient of a vector-function $\mathbf{f}$ on the triangle $\mathbf{T}$ is defined as $\nabla\mathbf{f}|_T = \sum_{k\in T}\mathbf{f}_k\nabla\varphi_k$ where the piece-wise linear functions φ_k form the standard basis.

DOI: 10.1002/fld

The weights σ_i and σ_k are defined depending on the position of points $\mathbf{r}_{ik}^{(1)}$ and $\mathbf{r}_{ik}^{(6)}$ on the segments $\left[D_i^1 D_i^2\right]$ and $\left[D_k^1 D_k^2\right]$, respectively (Figure 3 (left)). For instance, if the point $\mathbf{r}_{ik}^{(6)}$ is denoted by P then $\sigma_k = \left|D_k^2 P\right| / \left|D_k^1 D_k^2\right|$.

Formulae (22) define unstructured analogs for the divided differences we need.

3.4.3. Quasi-1D reconstruction. Using (21) and (22), we can formulate the quasi-1D reconstruction as

$$\begin{aligned}
\boldsymbol{\Phi}_{ik}^L &= \boldsymbol{\Phi}_i - \frac{1}{30}\left[\sigma_i \nabla\boldsymbol{\Phi}|_{\mathrm{T1}^L} + (1-\sigma_i)\nabla\boldsymbol{\Phi}|_{\mathrm{T2}^L}\right]\cdot \mathbf{e}_{ik} + \frac{11}{60}\nabla\boldsymbol{\Phi}|_{\mathrm{T}^L}\cdot \mathbf{e}_{ik} + \frac{2}{5}(\boldsymbol{\Phi}_k - \boldsymbol{\Phi}_i) - \frac{1}{20}\nabla\boldsymbol{\Phi}|_{\mathrm{T}^R}\cdot \mathbf{e}_{ik} \\
\boldsymbol{\Phi}_{ik}^R &= \boldsymbol{\Phi}_k + \frac{1}{20}\nabla\boldsymbol{\Phi}|_{\mathrm{T}^L}\cdot \mathbf{e}_{ik} - \frac{2}{5}(\boldsymbol{\Phi}_k - \boldsymbol{\Phi}_i) - \frac{11}{60}\nabla\boldsymbol{\Phi}|_{\mathrm{T}^R}\cdot \mathbf{e}_{ik} + \frac{1}{30}\left[\sigma_k \nabla\boldsymbol{\Phi}|_{\mathrm{T1}^R} + (1-\sigma_k)\nabla\boldsymbol{\Phi}|_{\mathrm{T2}^R}\right]\cdot \mathbf{e}_{ik}
\end{aligned} \tag{23a}$$

Definition 2

We say that a reconstruction is *quasi-1D of Mth order* if it transforms to the *M*th-order high-order 1D reconstruction on TS-meshes.

The schemes based on the reconstruction (23a) or other approximations on unstructured stencils that meet the definition of quasi-1D reconstruction of the fifth order are further referred to as the *EBR5 schemes*.

Analogously, if we imply a lower-order 1D reconstruction (21b), we can build an EBR3 scheme of the third highest theoretically reachable order by using the quasi-1D reconstruction:

$$\begin{aligned}
\boldsymbol{\Phi}_{ik}^L &= \boldsymbol{\Phi}_i + \frac{1}{3}(\boldsymbol{\Phi}_k - \boldsymbol{\Phi}_i) + \frac{1}{6}\nabla\boldsymbol{\Phi}|_{\mathrm{T}^L}\cdot \mathbf{e}_{ik} \\
\boldsymbol{\Phi}_{ik}^R &= \boldsymbol{\Phi}_k - \frac{1}{3}(\boldsymbol{\Phi}_k - \boldsymbol{\Phi}_i) - \frac{1}{6}\nabla\boldsymbol{\Phi}|_{\mathrm{T}^R}\cdot \mathbf{e}_{ik}.
\end{aligned} \tag{23b}$$

3.4.4. Stencil of quasi-1D reconstruction. The set of nodes $S_{ik}^{1D} = \left\{\mathbf{r}_{ik}^{(1)}, \mathbf{r}_{ik}^{(2)}, \mathbf{r}_{ik}^{(3)} \equiv \mathbf{r}_i, \mathbf{r}_{ik}^{(4)} \equiv \mathbf{r}_k, \mathbf{r}_{ik}^{(5)}, \mathbf{r}_{ik}^{(6)}\right\}$ cannot be considered as a reconstruction stencil for an arbitrary unstructured triangular or tetrahedral mesh because, in general, these nodes are not the mesh vertices. In the case considered in Sections 3.4.1 and 3.4.2, for quasi-1D reconstruction (23a), the real stencil of reconstruction is the set of the mesh nodes (Figure 4)

$$S_{ik}^{Q1D} = \left\{B_i^2, C_i^2, B_i^1, C_i^1, B_i, C_i, A_i, A_k, B_k, C_k, B_k^1, C_k^1, B_k^2, C_k^2\right\}.$$

In other words, the reconstruction stencil includes, besides the mesh nodes $\mathbf{r}_i$ and $\mathbf{r}_k$, the vertices of the two *first-level supporting triangles* $\mathrm{A}_k\mathrm{B}_k\mathrm{C}_k$ and $\mathrm{A}_i\mathrm{B}_i\mathrm{C}_i$, and vertices of the four *second-level supporting triangles* $A_k^1 B_k^1 C_k^1, A_k^2 B_k^2 C_k^2, A_i^1 B_i^1 C_i^1$, and $A_i^2 B_i^2 C_i^2$. Totally, it can contain up to 14 vertices.

The stencil S_i^{Q1D} is the *stencil of quasi-1D reconstruction*.

For an unstructured tetrahedral mesh, the stencil of quasi-1D reconstruction is composed analogously. The difference is that the stencil S_i^{Q1D} for the calculation of the numerical flux h_{ik} in the 3D case consists, besides the mesh nodes $\mathbf{r}_i$ and $\mathbf{r}_k$, of vertices of the two *first-level* and six (three from each side of edge *ik*) *second-level supporting tetrahedrons*. In the 3D case, a *stencil of quasi-1D reconstruction* can contain at most 26 vertices.

DOI: 10.1002/fld

3.5. Economical quasi-1D reconstruction and new simplified EBR schemes

Let us consider the determination of values $\mathbf{\Phi}_{ik}^{L}$ and $\mathbf{\Phi}_{ik}^{R}$ taken from the different sides of cell interface in the framework of the method described previously. Recall that to derive formulae (23a), we replace the first divided differences in (21) with the gradients defined on the corresponding triangles. At the same time, obviously, the formula (21) can be implemented directly if we determine the values $\mathbf{\Phi}_{ik}^{(s)}$ at all the points $\mathbf{r}_{ik}^{(s)}$, $s = \overline{1,6}$. Let us elaborate on this idea.

First, note that the reconstruction (23b) of EBR3 schemes remains the same if we define the missing values $\mathbf{\Phi}_{ik}^{(2)}$ and $\mathbf{\Phi}_{ik}^{(5)}$ at the points $\mathbf{r}_{ik}^{(2)}$ and $\mathbf{r}_{ik}^{(5)}$ in (21b) as linear interpolations on the segments $[\mathbf{B}_i, \mathbf{C}_i]$ and $[\mathbf{B}_k, \mathbf{C}_k]$ and then calculate the corresponding first divided differences explicitly. Let us build a similar procedure for the evaluation of values $\mathbf{\Phi}_{ik}^{(1)}$ and $\mathbf{\Phi}_{ik}^{(6)}$ at the points $\mathbf{r}_{ik}^{(1)}$ and $\mathbf{r}_{ik}^{(6)}$ based on linear interpolations that does not compromise the scheme accuracy. Let us demonstrate the procedure on the example of the value $\mathbf{\Phi}_{ik}^{(1)}$ to be defined at the point $\mathbf{r}_{ik}^{(1)}$.

For a node i, define the set of nodes $N_2(i)$ that are connected with the node i by two mesh edges and not by one mesh edge. Thus, the set $N_2(i)$ includes all the 'second-level' neighbors of the node i. Then consider a 'shell' consisting of all the mesh edges (mesh faces in 3D) connecting the nodes of $N_2(i)$. Leaving aside boundary regions, we can assert that there exists at least one edge (face in 3D) of this 'shell' that intersects the line $\mathbf{E}$ from the left of node i. In the case of a structured mesh, these edges form a closed contour around the node i, and there is only one intersection of this contour with the line $\mathbf{E}$ from the left of the node i. Take this intersection point as the point $\mathbf{r}_{ik}^{(1)}$. If the mesh is unstructured, there can be several intersections, and any of them can be taken as the point $\mathbf{r}_{ik}^{(1)}$. When the point $\mathbf{r}_{ik}^{(1)}$ is defined, we calculate the value $\mathbf{\Phi}_{ik}^{(1)}$ by the linear interpolation on the edge (face in 3D) containing $\mathbf{r}_{ik}^{(1)}$.

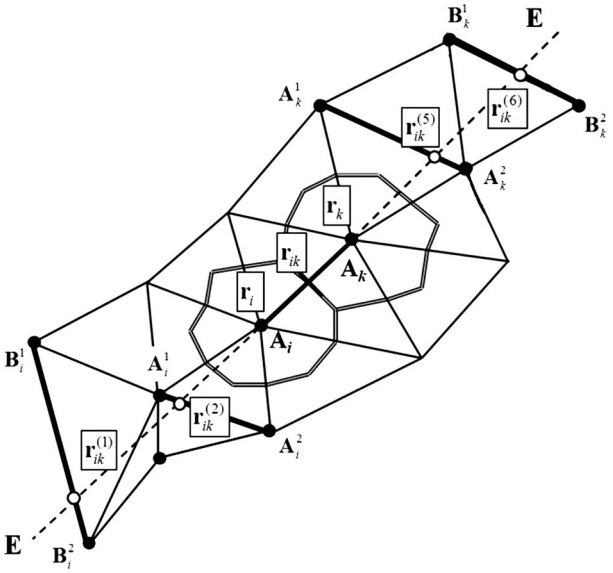

Figure 5. Stencil of economical quasi-one-dimensional reconstruction for an arbitrary triangular mesh.

Table I. A number of stencil nodes used in the economical reconstruction of fluxes.

	A number of stencil nodes	
Reconstruction	2D	3D
Basic	Up to 14	Up to 26
Economical	10	14

2D, two-dimensional; 3D, three-dimensional.

DOI: 10.1002/fld

Figure 5 illustrates the resulting procedure of economical reconstruction and shows its economical stencil $S_{ik}^{Q1D\ Ec}$ consisting of 10 nodes (in 2D case): $S_{ik}^{Q1D\ Ec} = \left\{B_i^1, B_i^2, A_i^1, A_i^2, A_i, A_k, A_k^1, A_k^2, B_k^1, B_k^2\right\}$.

A number of the stencil nodes needed for the determination of each couple of fluxes $\mathbf{\Phi}_{ik}^L$ and $\mathbf{\Phi}_{ik}^R$ is given in Table I. Thus, in 3D case, the economic reconstruction reduces the number of stencil points needed for the flux calculation almost twice. Note also that the size of the economical stencil is minimal possible required for quasi-1D reconstruction of EBR schemes.

The schemes based on the reconstruction on the economical stencil form a new subfamily of EBR schemes that are further referred to as the *SEBR schemes*. As it is shown further, the SEBR schemes provide practically the same accuracy as other EBR schemes of the corresponding theoretically reachable order, but gain noticeably in computational costs.

3.6. EBR scheme in boundary region

A common problem for the schemes operating on wide stencils is that near the boundary it is impossible to define the appropriate stencil. The most widespread solution in this case is to reduce the stencil and, correspondingly, the scheme order of accuracy.

When we use the scheme of reduced order near the walls, it is important to keep the scheme exactness on linear functions. Thus, if there is no stencil for the EBR5 or SEBR5 schemes, we use the lower-accuracy EBR3 schemes. If there is no stencil for the EBR3 schemes, we use the following scheme modification. Let, for example, the triangle T^L (Figure 4) cannot be found. Define the values $\mathbf{\Phi}_{ik}^L$ and $\mathbf{\Phi}_{ik}^R$ as

$$\mathbf{\Phi}_{ik}^L = \frac{1}{2}(\mathbf{\Phi}_i + \mathbf{\Phi}_k)$$
$$\mathbf{\Phi}_{ik}^R = \mathbf{\Phi}_k - \frac{1}{3}(\mathbf{\Phi}_k - \mathbf{\Phi}_i) - \frac{1}{6}\nabla\mathbf{\Phi}|_{\mathrm{T}^R} \cdot \mathbf{e}_{ik}.$$

This approximation is exact on linear functions and in practice provides stable computations.

If the node i or k is located in the vicinity of a boundary with some non-reflecting boundary conditions, the first-order scheme can be used. When at least one of these nodes lays on a solid wall, to provide a stable computation, we use the Roe solver (8) and the reconstruction of conservative variables even if we reconstruct fluxes in internal regions.

3.7. Accuracy of EBR schemes on arbitrary triangular/tetrahedral meshes

Numerous numerical results suggest that EBR schemes on unstructured meshes in the case of barycentric cells possess the second-order of accuracy. A strict proof of this fact is still lacking. We think that this follows from the first order of approximation coupled with exactness on linear functions of flux variables $\mathbf{\Phi}_{ik}^L$ and $\mathbf{\Phi}_{ik}^R$ in the middle of the mesh edge ik.

At the same time, as shown previously, there is a special class of meshes, namely, TS-meshes, providing the highest theoretically reachable (fifth and sixth) order of accuracy for EBR schemes. Although TS-meshes are not so widely used in practice, the property of high accuracy on TS-meshes appears useful. For instance, 2D mesh generators are able to produce unstructured meshes containing large structured blocks of triangles. Inside these domains, a mesh is often close to translationally symmetric. This fact provides high quality of computations in total. In the test cases presented in the succeeding text, we specially avoid such 'quasi-structured' meshes and use really unstructured meshes. Unfortunately, popular 3D mesh generators do not offer 'quasi-structured' meshes. So the development of such mesh generators would be a significant contribution to the high-accuracy numerical simulations performed with the help of EBR schemes.

DOI: 10.1002/fld

4. NUMERICAL RESULTS

4.1. Evolution of the 2D Gaussian pulse

To estimate experimentally the order of EBR schemes, we consider the initial-value problem for the linearized Euler equations with the initial data:

$$\rho(x,y)|_{t=0} = p(x,y)|_{t=0} = Ae^{-\frac{\ln 2}{b^2}(x^2+y^2)}$$
$$u(x,y)|_{t=0} = v(x,y)|_{t=0} = 0$$

The background field is $\overline{\rho} = 1, \quad \overline{u} = \overline{v} = 0, \quad \overline{p} = 1/\gamma$.

The initial shape of the Gaussian pulse is determined by the amplitude $A = 0.5$ and the half-width $b = 12$.

We consider two types of triangular unstructured meshes: TS-meshes composed of regular triangles and unstructured meshes generated by Gmsh generator. Fragments of such meshes with the corresponding barycentric and orthocentric cells are shown in Figure 6.

For the time integration, we use the explicit linear fifth-order Runge–Kutta method.

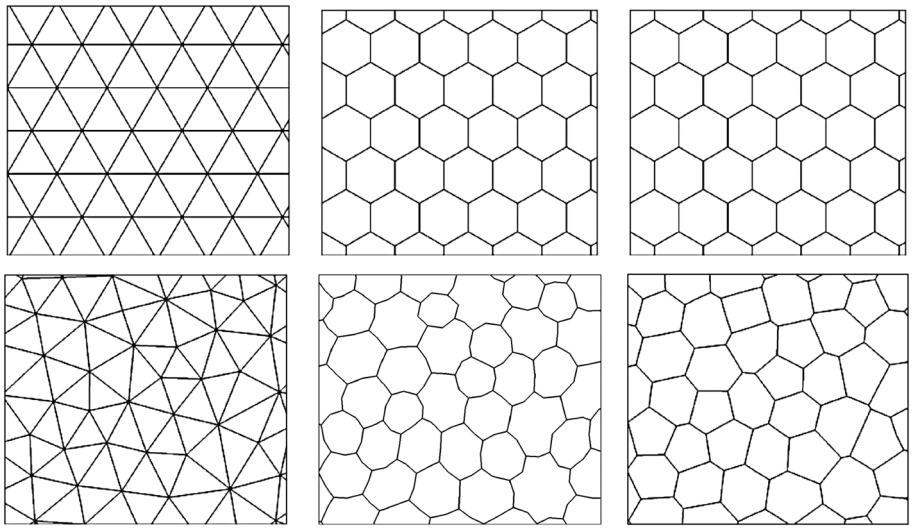

Figure 6. Translationally symmetric (upper row) and unstructured (lower row) meshes: mesh fragments (left column) and corresponding barycentric (middle column) and orthocentric (right column) cells.

Table II. The errors and the estimated order of accuracy in the case of translationally-symmetric meshes in C-norm and L_1-norm.

Scheme:	P2	EBR3	EBR5 = SEBR5	FC
Norm C	2.98	2.98	4.95	1.99
	7.721×10^{-4}	8.206×10^{-4}	3.122×10^{-5}	2.514×10^{-3}
	1.012×10^{-4}	1.079×10^{-4}	1.013×10^{-6}	6.459×10^{-4}
	1.282×10^{-5}	1.369×10^{-5}	—	1.625×10^{-4}
Norm L_1	2.99	2.99	4.93	2.01
	1.238×10^{-4}	1.314×10^{-4}	4.699×10^{-6}	3.798×10^{-4}
	1.588×10^{-5}	1.681×10^{-5}	1.537×10^{-7}	9.455×10^{-5}
	1.997×10^{-6}	2.110×10^{-6}	—	2.355×10^{-5}

EBR, edge-based reconstruction; SEBR, simplified EBR; FC, flux corrector.

DOI: 10.1002/fld

Table III. The errors and the estimated order of accuracy in the case of unstructured meshes with the use of barycentric and orthocentric control volumes in C-norm (upper table) and L_1-norm (lower table).

Norm:	C-norm				
Scheme:	P2	EBR3	EBR5	SEBR5	FC
Barycentric cells	2.94	2.28	1.76	1.72	1.99
	9.633×10^{-4}	1.122×10^{-3}	5.315×10^{-4}	5.530×10^{-4}	2.509×10^{-3}
	1.243×10^{-4}	1.714×10^{-4}	1.028×10^{-4}	1.066×10^{-4}	6.347×10^{-4}
	1.620×10^{-5}	3.523×10^{-5}	3.039×10^{-5}	3.247×10^{-5}	1.594×10^{-4}
Orthocentric cells	2.97	0.92	1.06	1.06	
	1.035×10^{-3}	1.866×10^{-3}	1.596×10^{-3}	1.615×10^{-3}	
	1.329×10^{-4}	8.964×10^{-4}	1.213×10^{-3}	1.213×10^{-3}	
	1.695×10^{-5}	4.754×10^{-4}	5.821×10^{-4}	5.798×10^{-4}	
Norm:			L_1-norm		
Scheme:	P2	EBR3	EBR5	SEBR5	FC
Barycentric cells	2.99	2.94	2.05	2.03	2.01
	1.449×10^{-4}	1.204×10^{-4}	1.931×10^{-5}	2.143×10^{-5}	3.690×10^{-4}
	1.849×10^{-5}	1.578×10^{-5}	4.048×10^{-6}	4.549×10^{-6}	9.157×10^{-5}
	2.323×10^{-6}	2.043×10^{-6}	9.780×10^{-7}	1.113×10^{-6}	2.272×10^{-5}
Orthocentric cells	2.97	1.11	0.93	0.93	
	1.545×10^{-4}	1.500×10^{-4}	9.567×10^{-5}	9.743×10^{-5}	
	1.967×10^{-5}	4.974×10^{-5}	5.131×10^{-5}	5.179×10^{-5}	
	2.483×10^{-6}	2.293×10^{-5}	2.699×10^{-5}	2.716×10^{-5}	

EBR, edge-based reconstruction; SEBR, simplified EBR; FC, flux corrector.

To estimate the scheme accuracy, the computations are performed on three meshes with the cell diameter approximately equal to 2, 1, and 0.5. The half-width $b=12$ is resolved on 6, 12, and 24 cells correspondingly.

The scheme accuracy is evaluated at the time moment $t=40$. The corresponding numerical results (Tables II and III) are given in terms of the errors $e_h=\|\rho_h-\rho_{ex}\|$ in the computation of density ρ_h with respect to its exact value ρ_{ex} in the norms L_1 and C. The accuracy order n is estimated using the formula $n=\frac{\ln e_{coarse}-\ln e_{fine}}{\ln 2}$, where e_{coarse} and e_{fine} are the errors obtained on the two meshes with the smallest steps.

The EBR schemes are compared with the quadratic-polynomial-based vertex-centered FV scheme (denoted here as P2) of the third order of accuracy [37] and with the FC scheme[‖] providing the third order of accuracy for steady problems [21].

As it is seen in Table II, on the mesh that consists of regular triangles (TS-mesh, Figure 6), the schemes EBR3 and EBR5 exhibit the third and the fifth order of accuracy correspondingly. This fact is in full agreement with the theoretical results of Section 3.3. The result obtained by the scheme EBR5 on the mesh with the smallest step is not given because of the insufficient accuracy in exact-value calculation. The FC scheme exhibits the second order of accuracy theoretically expected on unsteady problems.

On all the meshes in use, the quadratic-polynomial scheme P2 shows its theoretical third order of accuracy. In contrast to the EBR schemes, here, we consider the averaged values over cells built around the mesh nodes.

On unstructured meshes (Figure 6), both EBR3, EBR5, and FC schemes demonstrate the second order for barycentric cells, while for orthocentric cells – the first order only. However, the order of accuracy characterizes the scheme accuracy in asymptotics and is not always representative for a fixed mesh in use. In this sense, it is important to analyze not only the order of accuracy but also the values of errors. For instance, the scheme EBR3 on barycentric cells turns out to be close (both in accuracy and order) to the polynomial scheme P2 (Table III), while the scheme EBR5 exhibits only the second order of accuracy. At the same time, the values of errors in the EBR5 case are significantly smaller. The explanation of this fact may be the following. For the mesh in use, the

[‖]For calculating gradients in the FC scheme, we use cubic-polynomial reconstruction.

DOI: 10.1002/fld

highest terms of scheme error, that is, the terms of second order of vanishing, generally appear smaller than the terms of third order. The scheme EBR5 damps the third-order terms, in contrast to the schemes P2 and EBR3. This phenomenon has been investigated in [38] for 1D case. The FC scheme demonstrates its second order on unsteady problems, however produces the error significantly larger than the EBR3 scheme.

Table III shows that the usage of orthocentric cells on unstructured meshes lowers accuracy. However, this type of cells is needed in boundary layers. Moreover, it is possible to combine the cells of different types within one computation, in order to gain the advantages of both in different regions.

The results obtained with the economical reconstruction are close to those obtained with the basic version of reconstruction. It is expectable because we still keep two main properties – the exactness on linear functions and the continuous transformation to the high-order scheme on TS-meshes.

4.2. Evolution of 3D Gaussian pulse

Let us consider a similar test case in the 3D formulation for unstructured tetrahedral meshes. As initial conditions, we take

$$\rho(x,y,z)|_{t=0} = p(x,y,z)|_{t=0} = Ae^{-\frac{\ln 2}{b^2}\left(x^2+y^2+z^2\right)}$$
$$u(x,y,z)|_{t=0} = v(x,y,z)|_{t=0} = w(x,y,z)|_{t=0} = 0.$$

Fix the Gaussian half-width $b=6$ and the amplitude $A=1/2$. The scheme accuracy is estimated at the time moment $T=20$.

For the computations, we use the meshes of two types. The first type is quasi-uniform unstructured meshes with the mesh step approximately equal to 1, 0.5, and 0.25; the second type is TS-meshes. The TS-mesh in use is built according to the following procedure. First, we take the structured mesh consisting of parallelepipeds with the coordinates of vertices for a coarser mesh

Table IV. The errors and the estimated order of accuracy for TS meshes with the use of barycentric and orthocentric control volumes in C-norm and L_1-norm.

Scheme:	EBR3		EBR5		FC
Cells:	Barycentric	Orthocentric	Barycentric	Orthocentric	Barycentric
Norm C	2.79	2.94	4.84	4.85	2.06
	6.71×10^{-3}	2.64×10^{-3}	7.41×10^{-4}	1.44×10^{-4}	1.15×10^{-2}
	9.71×10^{-4}	3.46×10^{-4}	2.63×10^{-5}	4.96×10^{-6}	2.74×10^{-3}
Norm L_1	2.85	2.88	4.88	4.91	1.96
	1.66×10^{-3}	7.71×10^{-4}	1.59×10^{-4}	3.83×10^{-5}	3.12×10^{-3}
	2.31×10^{-4}	1.05×10^{-4}	5.38×10^{-6}	1.26×10^{-6}	8.03×10^{-4}

TS, translationally symmetric; EBR, edge-based reconstruction; FC, flux corrector.

Table V. The errors and the estimated order of accuracy for unstructured meshes with the use of barycentric control volumes in C-norm and L_1-norm.

Scheme:	EBR3	EBR5	SEBR5	FC
Norm C	2.65	2.41	2.00	2.06
	4.794×10^{-3}	1.548×10^{-3}	1.822×10^{-3}	1.391×10^{-2}
	6.538×10^{-4}	3.898×10^{-4}	4.358×10^{-4}	3.209×10^{-3}
	1.042×10^{-4}	7.343×10^{-5}	1.089×10^{-4}	7.678×10^{-4}
Norm L_1	2.82	2.06	2.06	1.90
	7.233×10^{-4}	2.194×10^{-4}	2.497×10^{-4}	2.348×10^{-3}
	9.691×10^{-5}	4.426×10^{-5}	5.149×10^{-5}	6.016×10^{-4}
	1.370×10^{-5}	1.061×10^{-5}	1.237×10^{-5}	1.505×10^{-4}

EBR, edge-based reconstruction; SEBR, simplified EBR; FC, flux corrector.

DOI: 10.1002/fld

and $\mathbf{C}_{ijk} = \frac{1}{2}\begin{pmatrix} i + 0.33j + 0.16k \\ -0.27i + j + 0.4k \\ 0.15i - 0.22j + k \end{pmatrix}$ for a finer one. Then we decompose all the parallelepipeds into tetrahedrons using the NGD-method [30].

The results of accuracy estimations are collected in Tables IV and V. In general, they confirm the conclusions made on the base of 2D test predictions presented in the previous section. On TS-meshes, the EBR3 scheme exhibits the third order of accuracy, the EBR5 scheme – the fifth order of accuracy that is their highest theoretically possible orders. A slightly better accuracy is reached in the case of orthocentric cells because of the better shapes of these cells.

On quasi-uniform unstructured meshes with barycentric cells, the EBR3 and EBR5 schemes are of the second order of accuracy. A remarkable detail is that the estimated order of EBR3 scheme is close to third and a little higher than the order of EBR5 scheme, while in the case of EBR5 scheme the errors are smaller. As expected for unsteady problems, the FC scheme demonstrates the second order of accuracy while producing significantly larger errors than the EBR schemes under consideration.

4.3. Analysis of computational costs

In this paragraph, we compare the SEBR schemes with quadratic-polynomial-based finite-volume schemes and flux correction scheme [21] in terms of the number of operations in 2D case. Suppose that we consider the 2D Euler equations so the number of unknown variables is equal to 4. Denote the number of mesh nodes by $\mathrm{N_n}$ and the number of mesh edges by $\mathrm{N_e}$. For consistency, we consider a polynomial-based scheme in vertex-centered formulation and assume that each cell face ∂C_{ik} consists only of one segment.

We estimate addition and multiplication as 1 operation each, division as four operations, and square root calculation as eight operations, which corresponds to modern computers. We estimate the average number of nodes in the second-order polynomial stencil as 11.5, which corresponds to the polynomial construction method presented in [24].

The implementation of the *SEBR5 scheme* based on Huang solver includes the following:

- calculation of $\mathcal{F} = (\mathrm{F}, \mathrm{G})$ in the mesh vertices – $17 \times \mathrm{N_n}$ operations;
- calculation of $\mathbf{\Phi}_{ik}^{(\mathrm{s})} = \mathcal{F} \times \mathbf{n}_{ik}$ in the points of economical stencil $s = \overline{1, 10}$ for four variables at all the mesh edges – $3 \times 10 \times 4 \times \mathrm{N_e} = 120 \times \mathrm{N_e}$ operations;
- calculation of $\mathbf{\Phi}_{\mathrm{ik}}^{(1)}$, $\mathbf{\Phi}_{\mathrm{ik}}^{(2)}$, $\mathbf{\Phi}_{ik}^{(5)}$, and $\mathbf{\Phi}_{ik}^{(6)}$ in points $\mathbf{r}_{ik}^{(1)}$, $\mathbf{r}_{ik}^{(2)}$, $\mathbf{r}_{ik}^{(5)}$, and $\mathbf{r}_{ik}^{(6)}$ (Figure 5) by the linear interpolation on the values in the stencil nodes for four variables at all the mesh edges – $4 \times 4 \times 3 \times \mathrm{N_e} = 48 \times \mathrm{N_e}$ operations;
- calculation of the reconstructed variables $\mathbf{\Phi}_{ik}^{L}$ and $\mathbf{\Phi}_{ik}^{R}$ for four variables at all the mesh edges – $2 \times 9 \times 4 \times \mathrm{N_e} = 72 \times \mathrm{N_e}$ operations; and
- implementation of Huang solver at all the mesh edges – $\sim 145 \times \mathrm{N_e}$ operations.

Totally, using approximation $\mathrm{N_e} \sim 3\mathrm{N_n}$, we estimate the costs of the SEBR5 scheme as $1172 \times \mathrm{N_n}$.

For the *P2 scheme* based on quadratic-polynomials and Roe solver, we have the following:

- calculation of five polynomial coefficients for four variables in the mesh vertices – $4 \times 5 \times 23 \times \mathrm{N_n} = 460 \times \mathrm{N_n}$ operations;
- calculation of reconstructed variables in two Gaussian points for four variables at all the mesh edges – $2 \times 2 \times 4 \times 13 \times \mathrm{N_e} = 208 \times \mathrm{N_e}$ operations; and
- implementation of Roe solver in two Gaussian points at all the mesh edges – $\sim 2 \times 230 \times \mathrm{N_e} = 460 \times \mathrm{N_e}$ operations.

Totally, we estimate the costs of the vertex-centered P2 scheme as $2464 \times \mathrm{N_n}$.

Similar reasoning for the *FC scheme* based on quadratic-polynomials, using the reconstruction both for fluxes and conservative variables and the Roe solver, gives the following:

- calculation of $\mathcal{F} = (\mathbf{F}, \mathbf{G})$ in the mesh vertices – $17 \times \mathrm{N_n}$ operations;

DOI: 10.1002/fld

Table VI. The computational costs of EBR schemes in processing time.

EBR5 scheme:	LV6 (nodal gradients)	EBR5 (gradients on supporting triangles)	SEBR5 (economical stencil –finite differences)
Processing time (in seconds)	14.51	11.99	10.52

EBR, edge-based reconstruction; SEBR, simplified EBR.

Table VII. The computational costs of different schemes in processing time and number of operations.

Scheme		Low-order	EBR3	SEBR5	FC quadratic polynomials
Linear 3D problem, reconstruction for variables only	Approximate number of operations per node per one RK iteration	690	3010	4270	3375
	Processing time (in seconds):	11.39	14.65	17.98	14.85
Nonlinear 3D problem, reconstruction for both variables and fluxes	Approximate number of operations per node per ones RK iteration	540	4020	5630	7060
	Processing time (in seconds):	10.66	17.29	24.23	21.24

- calculation of two derivatives for four conservative variables and eight flux variables $\mathcal{F}$ in the mesh vertices – $(4+8)\times 2\times 23\times N_n = 552\times N_n$ operations;
- projection of the derivatives into edge direction – $2\times(4+8)\times 3\times N_e = 72\times N_e$ operations;
- calculation of $\mathbf{\Phi}_i = \mathcal{F}_i \mathbf{n}_{ik}$ and the same operation for the gradients – $2\times 2\times 4\times 3\times N_e = 48\times N_e$ operations;
- calculation of reconstructed value for the variables and fluxes at all the mesh edges – $2\times 3\times(4+4)\times N_e = 48\times N_e$ operations; and
- implementation of Roe solver at all the mesh edges – $\sim 170\times N_e$ operations.

Totally, we estimate the costs of the vertex-centered FC scheme as $1583\times N_n$. The FC-scheme costs can be reduced up to $1183\times N_n$ if we use the Huang solver like in the SEBR scheme. As a result, we find that the computational costs of FC and SEBR5 schemes are approximately the same.

Now, let us estimate the computational costs of EBR schemes experimentally. Tables VI and VII collect the results of experimental investigation of the schemes costs in terms of processing time in seconds and, in Table VII, in terms of numbers of operations per node per one Runge–Kutta iteration. The time for preprocessing is neglected. All the data are obtained for barycentric cells.

For the 2D case of Section 4.1, we examine three EBR schemes based on the 1D Riemann solver of Huang (10-11) with different types of quasi-1D reconstruction of fluxes. We take the unstructured mesh of 212444 nodes and run six time steps of three-stage Runge–Kutta method. The resulting computational costs are given in Table VI. We see that the SEBR5 scheme is the fastest among the three EBR schemes under consideration.

For the 3D case of Section 4.2, we examine the low-order vertex centered scheme, EBR3 and SEBR5 schemes, and compare them with the FC scheme. We use both nonlinear and linear formulations based on the Euler system and its linearized version. We take the unstructured mesh of 147338 nodes and run six time steps of three-stage Runge–Kutta method. When implementing the FC scheme, we have used the polynomial construction method [24] with the stencil of 28.5 nodes in average used for the gradient calculation. The experimental results on computational costs are given in Table VII.

The data of Table VII say that the FC scheme is slower than the EBR3 scheme but faster than the SEBR5 scheme even for nonlinear problem despite a larger number of operations needed. The last phenomenon is connected with the nodal-gradient calculations spending approximately half of total computational costs. The calculation of nodal gradients in the FC scheme is implemented as a matrix–vector product that treats all the variables simultaneously (20 variables totally – five conservative variables and 15 flux variables). This operation is highly efficient with regard to memory access.

DOI: 10.1002/fld

Note that in 3D formulation, the quadratic-polynomial-based FV schemes [7] are much more expensive than the EBR schemes because of the wide stencil and the necessity to calculate 10 polynomial coefficients at each mesh cell.

4.4. Acoustic wave scattering by the Gaussian-core vortex

Simulation of wave scattering by isolated vortices of different shapes is a widely used benchmark problem in computational aeroacoustics (CAA). For instance, for the Gaussian-core vortex in 2D this case was studied in [39].

We use this problem to estimate the order of EBR schemes as applied to the Euler equations linearized on a non-uniform background flow field. As the mean flow field, we take the Gaussian-core vortex. It is characterized by the Mach number $\mathrm{M}_v = (V_\theta)_{\max}/c_\infty$ where $(V_\theta)_{\max}$ is the maximal tangential velocity and c_∞ is the speed of sound far from the vortex core. The corresponding flow fields are given as

$$V_\theta = \frac{M_\mathrm{v}}{(1-\exp(-\alpha))r}\left(1-\exp\left(-\alpha r^2\right)\right), \qquad V_r(r) = 0$$
$$\frac{\partial p}{\partial r} = (\gamma p)^{1/\gamma}\ \frac{V_\theta^2}{r}, \tag{24}$$

where a is the vortex radius and r is the distance to the vortex center. The constant $\alpha = 1.256431$ is chosen so that the maximal tangential velocity is reached at the distance $r = a$. The last equation of (24) is solved numerically.

Cylindrical acoustic waves are generated by the acoustic source term

$$s(\mathbf{r},t) = A\exp\left(-\frac{\ln\ 2}{b^2}\left(\mathbf{r}-\mathbf{r_0}\right)^2\right)\ \sin(2\pi\nu t) \quad \mathbf{r} = (x,y)$$

where $b = 1$ and $A = 0.1$ are the Gaussian half-width and amplitude correspondingly, $\nu = 0.25$ is the frequency.

The computational domain is schematically depicted in Figure 7. The source center is placed at $\mathbf{r}_0 = (25,\ 20)$.

The problem is solved on three meshes with halving steps. The approximation order is estimated by comparing the instantaneous pressure fields obtained on the meshes with steps h, $2h$, $4h$ according to the formula

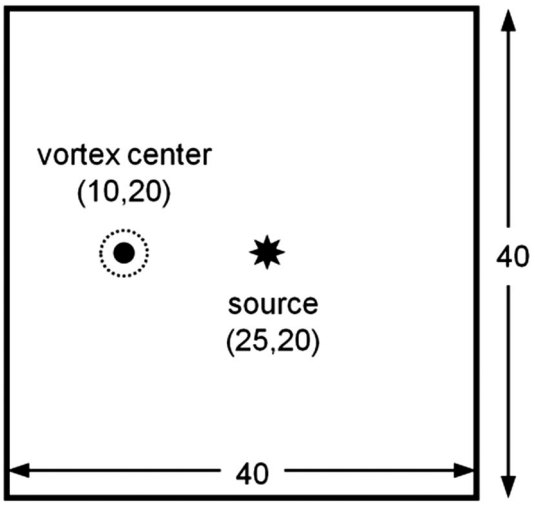

Figure 7. Scheme of the computational domain for the problem of acoustic wave scattering by the Gaussian-core vortex.

DOI: 10.1002/fld

Table VIII. The estimated order of accuracy.

	Norm C			Norm L_1			Norm L_2		
Time moments	1	2	3	1	2	3	1	2	3
'Cartesian' mesh	4.94	4.94	4.92	4.99	5.00	5.00	4.98	4.99	5.00
Quasi-uniform mesh	2.51	2.68	2.66	2.47	2.40	2.39	2.44	2.40	2.39
TS regular-triangular mesh	5.00	4.97	4.97	5.01	5.01	5.01	5.01	5.01	5.01

TS, translationally symmetric.

$$n \approx \frac{\ln\left\|p_h' - p_{4h}'\right\| - \ln\left\|p_h' - p_{2h}'\right\|}{\ln\ 2}$$

The calculations of corresponding discrepancies $\|\cdot\|$ in different norms are based only on the nodes of the coarsest mesh, which are common for all the three meshes in use. The integral norms L_1 and L_2 are evaluated on the subdomain $\{(x,y):\quad 0<x<20,\quad 10<y<30\}$.

The estimations are performed for three time moments: 1 – the wave does not reach the vortex, 2 – the wave is passing the vortex, 3 – the wave has passed the vortex.

For the simulations, we use the EBR5 scheme of the fifth theoretically reachable order of accuracy combined with the fifth-order explicit linear Runge–Kutta method for time integration. Three types of triangular meshes are as follows: (1) 'Cartesian'; (2) quasi-uniform 'acute-angled' (Figure 4, middle row); and (3) TS regular-triangular, participate in the experimental evaluation of accuracy.

The results collected in Table VIII confirm the fifth order of accuracy theoretically expected for the 'Cartesian' mesh and the TS mesh consisting of regular triangles. The orders estimated on the quasi-uniform mesh are significantly lower, although still noticeably higher than second.

4.5. Steady viscous nonconducting shock

In Sections 4.1–4.3, it is shown that for unsteady problems, the EBR schemes, being of the second order of accuracy as the FC scheme and comparable with it in computational costs, can give significantly better results. It is interesting now to compare the numerical results for steady problems where the FC scheme offers the third order of accuracy and, at the same time, to validate our implementation of this scheme.

Most of steady problems include walls, and thus, the quality of near-wall approximation may crucially influence the computational accuracy. To avoid this problem, we have chosen a steady problem without walls.

The viscous terms are approximated in the following way. At first, at all the mesh vertices, we calculate gradients of physical variables using the third-order interpolation polynomial. Then we

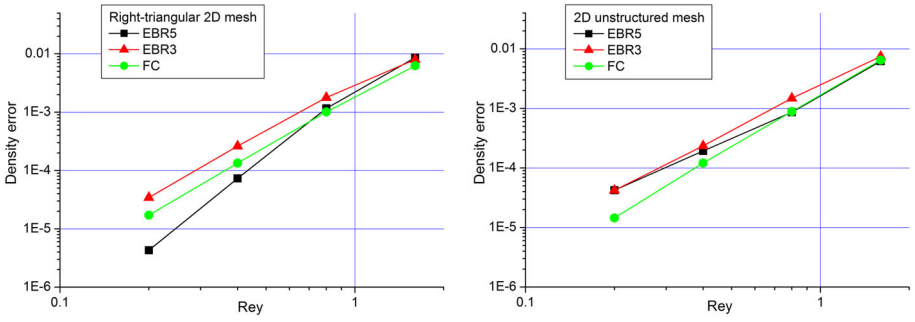

Figure 8. Convergence of solution error in two-dimensional (2D) case. EBR, edge-based reconstruction; FC, flux corrector.

DOI: 10.1002/fld

add these gradients to the convective fluxes and apply the same scheme that we use for the convection. The same technique, in particular, has been used in [40].

Let us consider the problem both in 2D and 3D formulations. At the input and output boundaries, we keep the exact solution. In 2D case, we use quasi-uniform triangular mesh generated by *gmsh*, in 3D case – by *Gambit*.

We estimated the accuracy without considering a possible slight shift between the numerical and exact solutions. To implement this, we determine the shift with the help of least square method.

Figure 8 (left) shows that on the uniform Cartesian mesh, the error of the FC scheme is approximately one-half of the error of EBR3 scheme, and both schemes exhibit their third order of accuracy. Note that in the present computations, we have used cubic polynomials for calculating convective fluxes. If we use quadratic polynomials, the results of FC and EBR3 practically coincide. The EBR5 scheme exhibits the fourth order of accuracy because the convective fluxes are calculated with the fifth order, while our approximation of viscous-terms gradients with the use of third-order polynomials coincides with the fourth-order central differences.

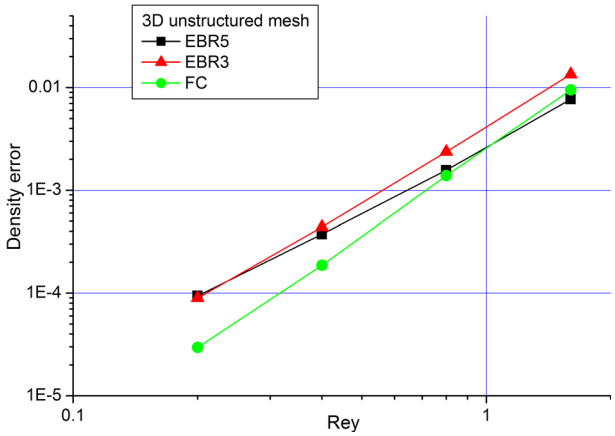

Figure 9. Convergence of solution error in three-dimensional (3D) case. EBR, edge-based reconstruction; FC, flux corrector.

Figure 10. VALIANT 'gap – turbulence interaction' case: SA IDDES ($\mathrm{Re} = 2 \cdot 10^4$), vorticity magnitude in the central cross-section. The Cartesian mesh of 8.4 million nodes and 49.5 million tetrahedrons.

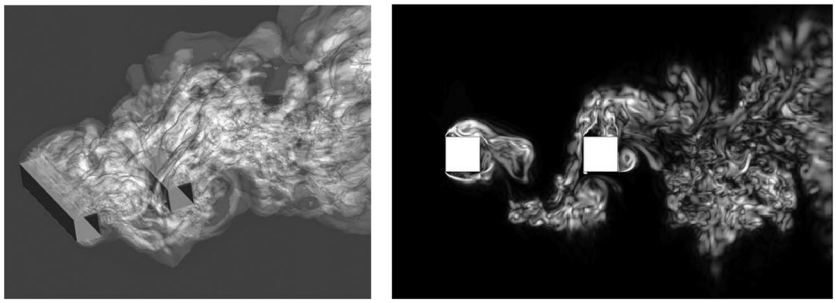

Figure 11. VALIANT 'two-cylinders' case: SA DDES ($\mathrm{Re} = 1.8 \cdot 10^5$), velocity magnitude isosurfaces (left) and vorticity magnitude (right) in the central cross-section. The structured non-Cartesian mesh of 13 million nodes and 72 million tetrahedrons.

DOI: 10.1002/fld

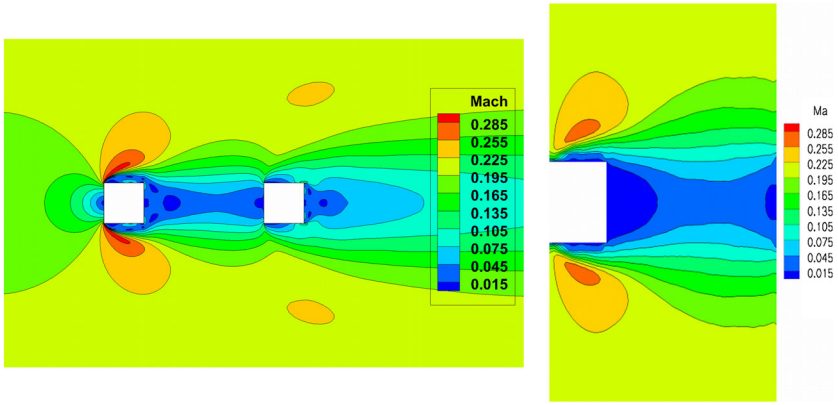

Figure 12. VALIANT 'two cylinders' case: time-averaged Mach number field in the central cross-section — numerical (left) and experimental (right) results.

Figure 13. Round jet – cylinder interaction: DNS ($\mathrm{Re} = 10^4$), absolute velocity field (left), SA IDDES ($\mathrm{Re} = 5.6 \cdot 10^4$), pressure time derivative (middle). Fragment of unstructured mesh of 100 million tetrahedrons (right).

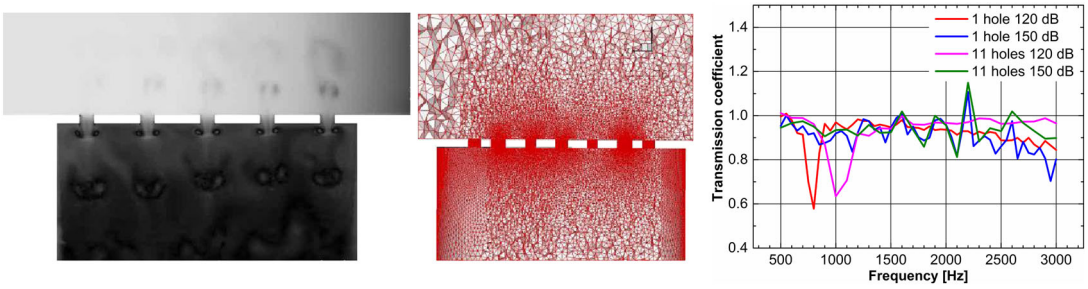

Figure 14. Perforated cell of acoustic liner: density field (left), fragment of unstructured mesh of 1.2 million nodes and 6.4 million tetrahedrons (middle), and estimated acoustic impedance (right).

On the unstructured triangular mesh (Figure 8, right), the FC scheme keeps the third order of accuracy, while the convergence of both EBR3 and EBR5 schemes degrades to the second order. In spite of this, on coarse meshes, the EBR5 and FC schemes produce very close results. Another remarkable detail, as in the linear case of Gaussian pulse simulation presented in Section 4.2, is that on a segment of coarse meshes, the EBR3 scheme exhibits the convergence similar to the third-order and thus to the convergence of the FC scheme.

In the 3D unstructured case, the convergence of solution error for all the schemes under study remains about the same as in the 2D case (Figure 9).

4.6. EBR schemes for real applications

The quasi-1D reconstruction underlying the EBR schemes has been also used for the approximation of the Spalart–Allmaras, k-ε, k-ω, and shear stress transport (SST) turbulence closure models,

DOI: 10.1002/fld

which allows us to apply these schemes for simulation of turbulent flows within the Reynolds-averaged Navier–Stokes (RANS) and hybrid detached eddy simulation (DES) approaches.

The EBR schemes and the corresponding quasi-1D developments have been implemented in the KIAM in-house code NOISEtte [41] exploiting the hybrid MPI-OpenMP parallelization model that has opened the doors to solving 3D applied problems.

In FP7 VALIANT Project, NOISEtte and, thus, the EBR schemes have been validated on two generic cases. Figures 10–12 show the numerical results of 'gap – turbulence interaction' and 'two cylinders' cases of VALIANT correspondingly. The details are given in [42–44].

The 3D simulations of round jet – cylinder interaction [45], the flow around 11-holes perforated cell of acoustic liner in a waveguide [46–48], are illustrated in Figures 13 and 14.

5. CONCLUSIONS

The paper considers the family of EBR schemes for solving systems of conservation laws with dominant advection as an extension of finite-difference methods to unstructured meshes. In the framework of finite-difference approach, the main idea of the EBR schemes construction consists in their formulation in terms of divided differences along the edge-based direction and the subsequent replacement of the differences by unstructured analogs.

On uniform grid-like meshes (TS-meshes), the EBR schemes provide the theoretical high order of accuracy (EBR3 and EBR5 schemes – up to the fourth and sixth order correspondingly). While not keeping very high order for arbitrary unstructured meshes, these schemes possess higher accuracy (compared with most second-order schemes) in terms of absolute errors owing to the quasi-1D high-order reconstruction. On coarse meshes used for real problems, the EBR5 schemes in many cases provide better results than the quadratic-polynomial-based FV scheme [7], which is significantly more expensive.

The recently developed FC scheme [21] presents a good alternative to the EBR3 and EBR5 schemes. It computationally costs approximately the same as the EBR schemes and provides the third order of accuracy for steady problems. For these problems, the EBR schemes give the results close to those obtained by the FC method only on coarse meshes, while on fine meshes, the accuracy of FC scheme is better. Basing on the test cases performed, we conclude that the EBR schemes are more accurate for unsteady problems. Another advantage of the EBR schemes is their high accuracy (up to the sixth order) on TS-meshes. This fact evokes ideas of generating meshes well suited for the EBR schemes, in particular, including domains of TS-meshes.

The gain in costs of the EBR schemes (with respect to the costs of most third-order schemes except, may be, the FC method) becomes especially significant for the algorithms equipped with shock-capturing techniques. This fact, in particular, has encouraged us to implement the quasi-1D reconstruction for the development of an efficient WENO-EBR scheme for unstructured meshes [49], [51],[**] which can be considered as a 'lite WENO' scheme. Before, in [29, 32], the quasi-1D TVD-method was discussed.

Generally, in the multidimensional unstructured case, many other useful techniques developed for 1D can be easily implemented in the framework of the quasi-1D approach. So far, we have extended this approach to the cell-centered formulation [50]. The generalization to unstructured meshes consisting of hexahedral and prismatic elements has been also carried out and firstly presented in [51].[††]

In the paper, we introduce a new EBR subfamily, namely, SEBR schemes. Thanks to the minimization of unstructured stencil, the SEBR schemes allow to reduce the computational costs of quasi-1D reconstruction in the 3D case approximately twice.

[**] The full paper is being prepared.
[††] The corresponding paper has been submitted.

DOI: 10.1002/fld

ACKNOWLEDGEMENTS

The work was partly supported by the European Commission within the 7th Framework Program (Project VALIANT under grant agreement number ACP8-GA-2009-233680) and Russian Foundation of Basic Research (Project 15-01-07911-a).

We thank Dr. Mikhail Surnachev who carefully read our manuscript and made a number of useful remarks.

REFERENCES

1. Jiang G, Shu C-W. Efficient implementation of weighted ENO schemes. *Journal of Computational Physics* 1996; **126**:202–228.
2. Liu X, Osher S, Chan T. Weighted essentially non-oscillatory schemes. *Journal of Computational Physics* 1994; **115**:200–212.
3. Friedrich O. Weighted essentially non-oscillatory schemes for the interpolation of mean values on unstructured grids. *Journal of Computational Physics* 1998; **144**:194–212.
4. Harten A, Engquist B, Osher S, Chakravathy S. Uniformly high order accurate essentially non-oscillatory schemes, III. *Journal of Computational Physics* 1987; **71**:231–303.
5. Serna S, Marquina A. Power ENO methods: a fifth-order accurate weighted power ENO method. *Journal of Computational Physics* 2004; **194**:632–658.
6. Dumbser M, Kaser M. Arbitrary high order non-oscillatory finite volume schemes on unstructured meshes for linear hyperbolic systems. *Journal of Computational Physics* 2007; **221**:693–723.
7. Dumbser M, Kaser M, Titarev VA, Toro EF. Quadrature-free non-oscillatory finite volume schemes on unstructured meshes for nonlinear hyperbolic systems. *Journal of Computational Physics* 2007; **226**:204–243.
8. Tsoutsanis P, Titarev VA, Drikakis D. WENO schemes on arbitrary mixed-element unstructured meshes in three space dimensions. *Journal of Computational Physics* 2011; **230**:1585–1601.
9. Cockburn B, Shu C-W. The Runge–Kutta discontinuous Galerkin method for conservation laws V: multidimensional systems. *Journal of Computational Physics* 1998; **141**:199–224.
10. Burbeau A, Sagaut P, Bruneau CH. A problem-independent limiter for high-order Runge–Kutta discontinuous Galerkin methods. *Journal of Computational Physics* 2001; **169**:111–150.
11. Krivodonova L. Limiters for high-order discontinuous Galerkin methods. *Journal of Computational Physics* 2007; **226**:879–896.
12. Biswas R, Devine K, Flaherty JE. Parallel adaptive finite element methods for conservation laws. *Applied Numerical Mathematics* 1994; **14**:255–284.
13. Wang ZJ, Liu Y, May G, Jameson A. Spectral difference method for unstructured grids II: extension to the Euler equations. *Journal of Scientific Computing* 2007; **32**:45–71.
14. Sun Y, Wang ZJ, Liu Y. High-order multidomain spectral difference method for the Navier–Stokes equations on unstructured hexahedral grids. *Communications in Computational Physics* 2007; **2**:310–333.
15. Premasuthan S, Liang C, Jameson A. Computation of flows with shocks using spectral difference scheme with artificial viscosity (AIAA paper 2010–1449), 2010.
16. Premasuthan S, Liang C, Jameson A. Computation of flows with shocks using the spectral difference method with artificial viscosity, II: modified formulation and local mesh refinement. *Computers & Fluids* 2014; **98**:122–133.
17. Qiu J-X, Shu C-W. Hermite WENO schemes and their application as limiters for Runge–Kutta discontinuous Galerkin method: one dimensional case. *Journal of Computational Physics* 2003; **193**:115–135.
18. Qiu J-X, Shu C-W. Runge–Kutta discontinuous Galerkin method using WENO limiters. *SIAM Journal of Scientific Computing* 2005; **26**:907–929.
19. Qiu J-X, Shu C-W. A comparison of troubled-cell indicators for Runge–Kutta discontinuous Galerkin methods using weighted essentially nonoscillatory limiters. *SIAM Journal of Scientific Computing* 2005; **27**:995–1013.
20. Qiu J-X, Shu C-W. Hermite WENO schemes and their application as limiters for Runge–Kutta discontinuous Galerkin method II: two dimensional case. *Computers & Fluids* 2005; **34**:642–663.
21. Katz A, Sankaran V. An efficient correction method to obtain a formally third-order accurate flow solver for node-centered unstructured grids. *Journal of Scientific Computing* 2012; **51**:375–393.
22. Nishikava H. First, second, and third order finite-volume schemes for advection–diffusion. *Journal of Computational Physics* 2014; **273**:287–309.
23. Nishikawa H. First, second, and third order finite-volume schemes for Navier–Stokes equations. In Proc. of 7th AIAA Theoretical Fluid Mechanics Conference, AIAA Aviation and Aeronautics Forum and Exposition 2014, AIAA Paper 2014–2091, Atlanta, GA, 2014.
24. Pincock BB, Katz A. High-order flux correction for viscous flows on arbitrary unstructured grids. In Proc. of 21st AIAA Computational Fluid Dynamics Conference, AIAA Paper 2011–2566, San Diego, California, June 2013.
25. Dalon Work C, Katz AJ. 'Aspects of the flux correction method for solving the Navier–Stokes equations on unstructured meshes' (AIAA 2015–0834) 53rd AIAA Aerospace Sciences Meeting, 2015.
26. Katz AJ, Work D. High-order flux correction/finite difference schemes for strand grids. *Journal of Computational Physics* 2015; **282**:360–380.

DOI: 10.1002/fld

27. Tong O, Katz AJ, Wissink AM, Sitaraman J. 'High-order methods for three-dimensional strand-cartesian grids' (AIAA 2015–0835) 53rd AIAA Aerospace Sciences Meeting, 2015
28. Debiez C. Approximations décentrées à faible dissipation pour des problèmes hyperboliques. *INRIA Report* 2811: 1996.
29. Dervieux A, Debiez C. Mixed element volume MUSCL methods with weak viscosity for steady and unsteady flow calculation. *Computers and Fluids* 1999; **29**:89–118.
30. Gourvitch N, Rogé G, Abalakin I, Dervieux A, Kozubskaya T. A tetrahedral-based superconvergent scheme for aeroacoustics. *INRIA Report* 5212, 2004.
31. Abalakin I, Dervieux A, Kozubskaya T. High accuracy finite volume method for solving nonlinear aeroacoustics problems on unstructured meshes. *Chinese Journal of Aeronautics* 2006; **19**:97–104.
32. Koobus B, Alauzet F, Dervieux A. Numerical algorithms for unstructured meshes. In *Computational Fluid Dynamics*, Magoul s F (ed.). CRC Press: London, New-York, 2011; 131–203.
33. Roe PL. Approximate Riemann solvers, parameter vectors and difference schemes. *Journal of Computational Physics* 1981; **43**:357–372.
34. Wu H, Wang L. Non-existence of third order accurate semi-discrete MUSCL-type schemes for nonlinear conservation laws and unified construction of high accurate ENO schemes. – In Proceedings of the *6th International Symposium on CFD*, Lake Tahoe, USA, September 4–8, 1995.
35. Huang LC. Pseudo-unsteady difference schemes for discontinuous solution of steady-state, one-dimensional fluid dynamics problems. *Journal of Computational Physics* 1981; **42**:195–211.
36. Abalakin I, Bakhvalov P, Kozubskaya T. Edge-based methods in CAA, *VKI Lecture Series*, March 25–28, 2013.
37. Kozubskaya T, Abalakin I, Dervieux A, Ouvrard H. Accuracy improvement for finite-volume vertex-centered schemes solving aeroacoustics problems on unstructured meshes. *16th AIAA/CEAS Aeroacoustics Conference*, Stockholm, Sweden, June 2010, AIAA paper 2010–3933, 2010.
38. Bakhvalov PA, Kozubskaya TK. Error structure of conservative 4-point finite-difference scheme on non-uniform meshes. Preprint of KIAM N 74, Moscow, 2014 — URL: http://library.keldysh.ru/preprint.asp?id=2014-74. (in Russian).
39. Colonius T, Lele S, Moin P. The scattering of sound waves by a vortex: numerical simulations. *Journal of Fluid Mechanics* 1994; **260**:271–298.
40. Nishikava H. A first-order system approach for diffusion equation. II: unification of advection and diffusion. *Journal of Computational Physics* 2010; **229**:3989–4016.
41. Abalakin IV, Bakhvalov PA, Gorobets AV, Duben AP, Kozubskaya TK. Parallel research code NOISEtte for large-scale CFD and CAA simulations. *Vychislitelnye Metody i Programmirovanie* 2012; **13**:110–125 (in Russian).
42. Kozubskaya T, Duben A, Knacke T, Thiele F, Kopiev V, Zaytsev M. Joint experimantal and numerical study of gapturbulence interaction, *19th AIAA/CEAS Aeroacoustics conference*, Berlin, Germany, May 2013, *AIAA paper 2013–2214*, 2013.
43. Abalakin I, Duben A, Gorobets A, Kozubskaya T. Fighting Against the Airframe Noise with Square Struts and Gaps in FP7 VALIANT Project – In Book of Abstracts of *International Workshop* '*Computational Experiment in AeroAcoustics*', *Svetlogorsk*, *Kaliningrad region*, *Russia*, *September 19–22*, *2012*, MAKS Press, Moscow, 2012, pp. 24–26.
44. Abalakin I, Bakhvalov P, Kozubskaya T. Edge-based reconstruction schemes for prediction of near field flow region in complex aeroacoustic problems. *International Journal of Aeroacoustics* 2014; **13**(3&4):207–234.
45. Duben A, Kopiev V, Kozubskaya T, Lukyanov N, Ostrikov N, Zaitsev M. Experimental and numerical investigations of structure of noise sources past cylinder – in book of abstracts of *international workshop* '*computational experiment in AeroAcoustics*', *svetlogorsk*, *Kaliningrad region*, *Russia*, *September 19–22*, *2012*, MAKS Press, ZaitsevMoscow, 2012, 55–57.
46. Duben AP, Kozubskaya TK, Mironov MA. Numerical investigation of resonators in the waveguide. *Fluid Dynamics* 2012; **47**(1):129–138.
47. Duben AP, Kozubskaya TK, Korolev SI, Maslov VP, Mironov AK, Mironova DA, Shakhporonov VM. Investigation of acoustic flow in the resonator throat: experiment and computational modeling. *Acoustical Physics* 2012; **58**(1):69–80.
48. Duben A, Kozubskaya T, Mironov M. Numerical investigation of resonators for acoustic liners, – in book of abstracts of trilateral Russian–French–German workshop '*computational experiment in aeroacoustics*', Svetlogorsk, September 22–25, 2010, M.: MAKS Press, 2010, 34–36.
49. Abalakin I, Bakhvalov P, Kozubskaya T. Edge-based reconstruction scheme and its WENO implementation for solving aerodynamics and aeroacoustics problems on unstructured tetrahedral meshes – in book of abstracts of *international workshop* '*computational experiment in AeroAcoustics*', *svetlogorsk*, *kaliningrad region*, *russia*, *September 19–22*, *2012*, MAKS Press, Moscow, 2012, 22–23.
50. Bakhvalov P. Quasi one-dimensional reconstruction scheme on convex polygonal meshes for solving aeroacoustics problems. *Matematicheskoe Modelirovanie* 2013; **25**(9):95–108 (in Russian).
51. Abalakin I, Bakhvalov P, Kozubskaya T. Edge-based reconstruction schemes: quasi-1D WENO implementation and extension to hybrid unstructured meshes. – in *Proceedings* of *HONOM 2015*, *European Workshop on High Order Nonlinear Numerical Methods for Evolutionary PDEs*: *Theory and Applications*, *March 16–20*, 2015, *University of Trento and CIRM-FBK*, *Italy*

DOI: 10.1002/fld